Controlling the electrokinetic transport of polyelectrolytes

Koen Vermeulen

Utrecht University

Master Thesis

Controlling the electrokinetic transport of polyelectrolytes through capillaries

Author:
Koen Vermeulen, BSc

Supervisors:
dr. M.F. Haase
H. Siegel, MSc

February 27, 2023

Abstract

Applying ultrathin polyelectrolyte (PE) coatings to porous substrates is an established way of to tailor the separation selectivity of membranes. The thickness and separation properties of adsorbed PEs on a charged porous substrate is governed by many variables such as the ionic strength, pH, and PE charge density. Furthermore, electric field assisted deposition of PEs onto porous substrates has been shown to provide additional control over the thickness and separation properties of the resulting membranes.

However, different electrokinetic transport mechanisms such as electroosmosis and electrophoresis occur simultaneously. Control over the transport dynamics of PEs in an electric field is thus essential for the formation of uniform PE coatings on porous substrates.

In this work, the electroosmotic flow (EOF) through glass capillaries is regulated by coating of the inner surface of the capillaries with poly(diallyldimethylammonium chloride) (pDADMAC). Depending on the ionic strength and the valency of the counterions during the coating procedure the EOF could be reversed or suppressed almost completely.

Based on this control over the EOF, electrophoretic mobility (μ_{EP}) measurements were performed on poly(allylamine hydrochloride) (PAH) as model PE. To this end, the experimental setup was first validated by the measurement of μ_{EP} of fluorescein. Subsequently, μ_{EP} of PAH was determined to be 43.9×10^{-9} $\mathrm{m^2\,V^{-1}\,s^{-1}}$, which is in good agreement with literature values.

The work presented here lays the foundation for introducing PEs into porous membrane matrices to control the formation of selective separation layers via electrokinetic transport.

Samenvatting

Veel delen in de wereld hebben te maken met een tekort aan bruikbaar zoetwater. Voor het zuiveren van water wordt veelal gebruik gemaakt van membranen. Membranen zijn poreuze materialen die een of meerdere opgeloste vervuilingen uit water kunnen scheiden. Dit soort membranen kunnen zelfs gebruikt worden om van zout water drinkbaar zoetwater te maken. Het is hiervoor belangrijk dat een membraan heel selectief is in het doorlaten van opgeloste deeltjes. Een manier om de selectiviteit van een membraan aan te passen is door het aanbrengen van een dunne deklaag die de selectiviteit van het membraan kan bepalen.

Een bestaande manier van het maken van selectieve deklagen is door membranen te voorzien van een laag polyelektrolyten. Polyelektrolyten zijn lange moleculen die erg veel positieve of negatieve ladingen hebben. Door deze ladingen blijven ze graag aan een oppervlak vastzitten. De manier waarop polyelektrolyten op een oppervlak vastzitten is afhankelijk van onder andere hoeveel andere geladen deeltjes, ionen, er aanwezig zijn, welke andere ionon er aanwezig zijn, en hoe zuur de oplossing is.

Voor het aanbrengen van een laag polyelektrolyten op een membraan kan gebruik gemaakt worden van een elektrisch veld. Polyelektrolyten zullen zich in een elektrisch veld verplaatsen van de plus naar de min pool, of andersom. Dit is afhankelijk van de soort lading van het polyelektrolyt (negatief of positief). Hoe polyelektrolyten zich precies verplaatsen in een elektrisch veld is afhankelijk van de sterkte van het elektrisch veld, hoeveel en welke ionon er aanwezig zijn, hoe zuur de oplossing is, en of het polyelektrolyt zich dicht bij een vast oppervlak bevindt.

In dit onderzoek is gekeken naar wat het effect is op het verplaatsen van polyelektrolyten in een elektrisch veld door dunne glazen buisjes genaamd capillairen. Wanneer een elektrisch veld wordt aangebracht over een capillair zal de vloeistof erin gaan stromen. Dit is afhankelijk van de aard van het oppervlak van de capillair. Tegelijkertijd zal het polyelektrolyt zich ook verplaatsen in het elektrische veld.

Er is gekeken naar hoe verschillende oppervlaktes van de capillair invloed hebben op de stroming van de vloeistof. Vervolgens is er ook onderzocht hoe we de verplaatsing van een polyelektrolyt door een capillair kunnen meten.

We ontdekten dat we de stroming van een vloeistof door een capillair kunnen tegengaan door het oppervlak van de capillair te bedekken met een laag van polyelektrolyten. Afhankelijk van hoeveel en welke ionen er in de oplossing aanwezig waren, konden we de stroming een beetje of bijna helemaal tegengaan. We hebben hierbij geleerd dat het polyelektrolyt dat we aanbrengen op het oppervlak zich verschillend aan het oppervlak hecht. De laag kon afhankelijk van de hoeveelheid en soort ionen aanwezig heel dun of veel dikker zijn.

We hebben ook kunnen meten hoe snel een polyelektrolyt zich beweegt

in het elektrisch veld afhankelijk van hoeveel ionon er aanwezig zijn. Hoe minder andere ionen er aanwezig zijn, hoe sneller het polyelektrolyt zich verplaatst.

Deze informatie willen we gebruiken om in de toekomst selectieve deklagen aan te brengen op membranen met behulp van elektrische velden.

Contents

1 Introduction

The world's increasing freshwater scarcity has led to an increased interest in implementing membrane separation techniques for the removal of contaminates from water sources [1–3]. Membranes are semipermeable barriers that allow for the separation of two or more dissolved species [2, 4]. Membranes are used in wastewater treatment, water purification, and desalination as a versatile technology with low operational energy requirements [5, 6].

Applying ultrathin polyelectrolyte (PE) coatings to porous substrates is an established way to incorporate tunable separation selectivity of membranes [7]. For example, polyelectrolyte coatings can introduce size-selective separation of uncharged organic molecules [8]. PEs are long polymer chains that carry many positively or negatively charged groups [9]. Electrostatic interactions allow the adsorption of PEs on porous membranes or the layering of alternately charged PEs [6].

The adsorption of PEs is dependent on many factors including the charge density of the PE, ionic strength and pH of the PE solution, and the pore confinement of the substrate [10]. Electric field assisted adsorption of PEs has been shown to provide excellent control over the thickness of the adsorbed PE layer [11, 12]. Furthermore, the amount of adsorbed PE could also be controlled using an electric field [13–15]. The resulting PE layers were smooth and homogenous and resulted in increased separation properties and layer stability compared to PE coatings deposited without an electric field [4, 16, 17]. Electric field assisted build-up of PE layers also increased the adsorption rate of PEs compared to the conventional dip coating method [4, 12].

Electric field assisted adsorption of PE on a porous substrate relies on the electrokinetic transport of PEs. This can occur via different mechanisms such as electroosmosis and electrophoresis. The PE transport depends on many factors, for instance the electric field strength, the charge density of the PE, and the ionic strength and pH of the PE solution.

This research was motivated by the idea to use electric field assisted adsorption of PEs to grow separation layers at the interface of bicontinuous interracially jammed emulsion gels (bijel) (Figure 1). Bijels are made via self-assembly of silica colloids at the interface of two interwoven immiscible fluids, resulting in a kinetically stabilized emulsion gel [18]. Electrokinetic transport phenomena would facilitate the introduction of PEs into the bijel structure and allow adsorption of the PEs on the colloidal scaffold. To gain fundamental understanding of the transport dynamics governing the decoration of the bijel scaffold with a PE layer, this work aims to understand and control the transport of PEs through glass capillaries in an electric field as a minimal reference system. The use of glass capillaries ensures comparable surface chemistry to the bijel's silica scaffold. The role of electroosmosis and electrophoresis on the transport of charged molecules is investigated.

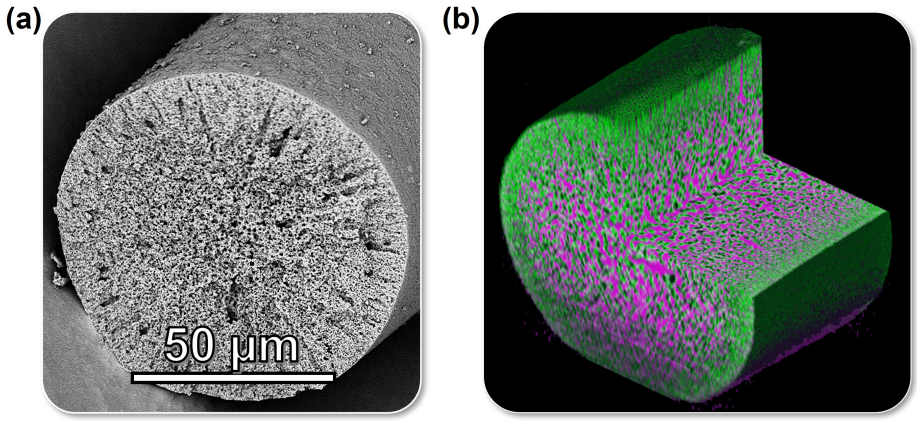

Figure 1: **(a)** SEM image showing the silica scaffold of a bijel fiber. **(b)** 3D reconstruction of confocal laser scanning microscopy images of a bijel fiber. Magenta indicates water domains and green indicates the silica scaffold. Images adapted from [18].

To this end, a capillary flow cell was built to study the electroosmotic flow (EOF) through glass capillaries coated with poly(diallyldimethylammonium chloride) (pDADMAC). The EOF was analyzed by tracking the migration of a neutral dye marker molecule and characterized by calculating the electroosmotic mobility from image analysis. This was complemented by employing streaming potential measurements to determine the zeta-potential of the capillaries under different coating conditions, and compared with EOF simulations.

Applying pDADMAC coatings allowed for control over the magnitude and direction of the EOF. Divalent counterions were identified to induce a conformational rearrangement of free and adsorbed pDADMAC. This resulted in a reduction of the zeta-potential and EOF of capillaries coated with pDADMAC at higher salt concentrations.

From EOF simulations we concluded that diffusion of analytes introduces a systematic overestimate of the electroosmotic mobility measured from EOF analysis.

Finally, the electrophoretic mobilities of charged (macro)molecules were measured using a home-made microscopy setup. Measurements were validated by determining the electrophoretic mobility of fluorescein as a well-documented reference molecule. The electrophoretic mobility of a model PE, poly(fluorescein isothiocyanate allylamine hydrochloride) (PAH-FITC), was determined at different ionic strengths. The absolute electrophoretic mobilities for fluorescein and PAH-FITC were determined to be 38.3×10^{-9} and 43.9×10^{-9} $\mathrm{m^2\,V^{-1}\,s^{-1}}$ respectively.

The fundamental understanding of electrokinetic transport of PEs presented here can hopefully serve as a stepping stone for future research into electric field assisted adsorption of PEs onto the silica scaffold of bijels.

2 Theoretical background

This chapter introduces the theoretical background on electrokinetic transport phenomena of charged species and polyelectrolytes. After discussing the general concept of electrokinetic transport phenomena an in depth treatment of the physical description of electroosmosis, streaming potential, and electrophoresis follows. Polyelectrolytes are defined, and their classification into weak and strong polyelectrolytes is explained. The adsorption of polyelectrolytes on charged substrates will be treated. Finally, the radius of gyration is discussed to describe the conformation of polyelectrolytes in solution, which can be measured using static light scattering.

2.1 Electrokinetic transport phenomena

Any charged species will experience a force in an electric field. The charged species will be accelerated according to Coulomb's law, which gives the force acting on two charged species depending on their charge and the distance between them (Eq. (1)). With F the Coulomb force, k_e the Coulomb constant, q_1 and q_2 the magnitude of the charges, and r the separation between the charges.

$$F = k_e \frac{q_1 q_2}{r^2} \tag{1}$$

For oppositely charged species the forces F_1 and F_2 point to each other as the interaction is attractive (Figure 2 (a)). The force acting on a positively charged particle in a homogeneous electric field of magnitude E is shown in Figure 2 (b). The direction of the corresponding acceleration a the particle experiences follows Newton's law. This basic principle of movement of free charges as a result of an applied electric field forms the foundation for all electrokinetic transport phenomena.

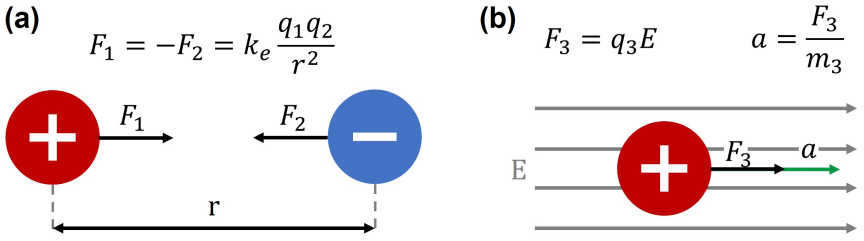

Figure 2: **(a)** Schematic representation of the Coulomb forces F_1 and F_2 acting on two oppositely charged particles. The particles represented as a red circle with a plus sign and a blue circle with a minus sign. The forces act in opposite direction because the interaction is attractive. **(b)** Schematic representation of the force acting on a positively charged particle in a homogeneous electric field, of strength E. The direction of the acceleration a that follows from Newton's law is indicated with the green arrow.

Electrokinetic transport phenomena refer to a family of phenomena involving electricity and a tangential movement of two phases with respect to each other [19]. The physical source of these phenomena lies in the so-called electrical double layer (EDL) that forms when a solid comes in contact with an electrolyte. The EDL consists of the charged surface at the solid and an equivalent amount of oppositely charged ions distributed in the solution. In the distribution of counterions around the solid, two regions can be distinguished. The first is a layer of tightly bound ions that have adsorbed to the charged surface known as the Stern layer (Figure 3) [20, 21]. Further away from the surface a diffuse region of counterions extends into the bulk. In the case of a moving surface some counterions in the diffuse region will stay attached to the surface and move along with it. The rest of the diffuse layer will not move along with the surface and is sheared off [22]. The boundary that separates these mobile and immobile regions of the diffuse layer is called the slipping plane (Figure 3). The electric potential at this plane, which is important to describe all electrokinetic phenomena, is defined as the zeta-potential (ζ) [19, 23].

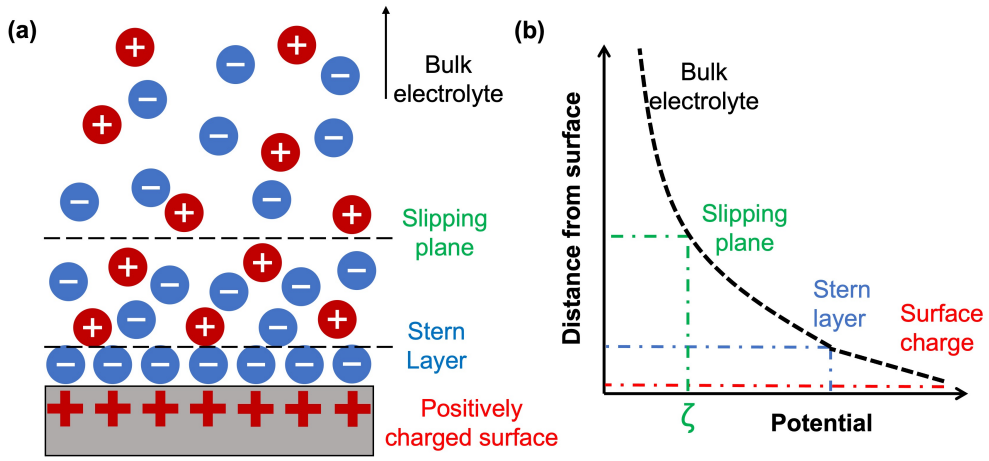

Figure 3: **(a)** Schematic representation of an electric double layer extending from a positively charged surface. Regions corresponding to the Stern layer, slipping plane, and bulk electrolyte are indicated. **(b)** Qualitative graph showing the electric potential as a function of the distance from the surface. The surface charge, Stern layer, and slipping plane are indicated. The potential at the slipping plane is defined as the zeta-potential, ζ.

The change in electric potential of a charged surface in contact with an electrolyte depends on the distance from the surface (Figure 3 (b)). The potential at the surface is fixed by the surface charge and decreases linearly over the thickness of the Stern layer. The Gouy-Chapman model describes the diffuse layer as an exponentially decaying function [19,24]. The previously introduced slipping plane is located in the diffuse layer.

It is the motion of the electrolyte relative to the charged surface at the

slipping plane that controls electrokinetic transport phenomena. These phenomena can be distinguished based on the driving force and the nature of the solid and liquid phases [25, 26]. In the following, the transport phenomena electroosmosis, streaming potential, and electrophoresis will be explained.

2.1.1 Electroosmosis

Applying an electric field across an electrolyte solution will cause the positive ions to move towards the cathode, and the negative ions towards the anode according to Coulomb's law. The opposite movement of these ions will cancel out such that no fluid flow will occur. When the same electrolyte is now confined in a narrow glass channel an EDL will extend from the surface into the solution [27,28]. Applying an electric field parallel to the surface will shear off excess counterions near the surface at the slipping plane (Figure 4). The movement of these counterions will induce a fluid flow due to drag forces exerted on the solvent. The fluid flow induced by movement of the ions is called electroosmosis [19,27,28]. As a consequence, a velocity profile develops that increases from zero at the wall to a maximum value v_{EO} at the center of the channel. The resulting velocity profile is called plug flow and the associated velocity v_{EO} is called the electroosmotic velocity [27].

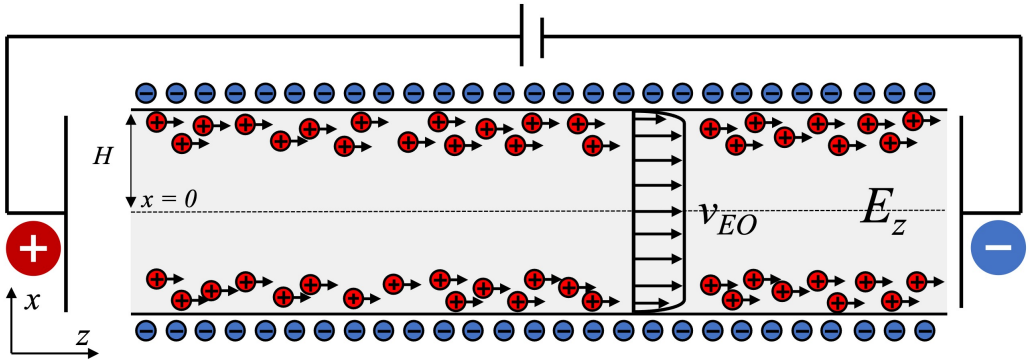

Figure 4: Schematic representation of electroosmosis in a channel with a negatively charged wall. Excess counterions in the electric double layer and the direction of their movement in the applied electric field E_z are indicated. The velocity profile in x-direction of the fluid flow is given.

The velocity profile in the stationary state can be calculated from a force balance between the Coulomb force and friction forces counteracting on a volume element in opposite directions. For a rectangular coordinate system and neglecting any additional forces this balance results in Equation (2) [19, 27].

$$E_z \rho = -\eta \frac{d^2 v_z}{dx^2} \tag{2}$$

E_z is the applied electric field parallel to the surface, ρ the charge density, η the viscosity of the solvent, and v_z the velocity in the direction parallel to the surface. Poisson's equation, Equation (3), describes the electric potential ψ that develops for a charge distribution ρ, with $\epsilon_0\epsilon_r$ the permittivity of the solution. It can be substituted for the charge density ρ in Equation (2) resulting in Equation (4).

$$\bigtriangledown^2\psi = -\frac{\rho}{\epsilon_0\epsilon_r} \tag{3}$$

$$E_z\epsilon_0\epsilon_r\frac{d^2\psi}{dx^2} = \eta\frac{d^2v_z}{dx^2} \tag{4}$$

Equation (4) can be integrated twice using the boundary conditions:

1. **for** $x = 0$: $d\psi/dx$ and dv_z/dx are zero as both the potential and the velocity reach a constant value

2. **at** $x = H$: $\psi = \zeta$ and $v_z = 0$ because $x = H$ is the slipping plane for which the potential is defined as the zeta-potential

The result of the integration gives the velocity profile in x-direction $v_z(x)$ (Equation (5)). However, here we are interested in the maximum velocity at the center of the channel, the electroosmotic velocity v_{EO}. In the bulk, electroneutrality demands $\psi = 0$, resulting in Equation (6) [19, 27]. The quantity μ_{EO} is called the electroosmotic mobility. It only depends on the zeta-potential ζ, and the permittivity $\epsilon_0\epsilon_r$ and viscosity η of the bulk. The electroosmotic mobility describes the velocity of the fluid under the influence of an electric field.

$$v_z(x) = \frac{\epsilon_0\epsilon_r}{\eta}E_z(\psi(x) - \zeta) \tag{5}$$

$$v_{EO} = -\frac{\epsilon_0\epsilon_r\zeta}{\eta}E_z = \mu_{eo}E_z \tag{6}$$

2.1.2 Streaming potential

In the previous section the presence of an EDL caused fluid flow when an electric field is applied over a narrow channel. The magnitude of the flow velocity is dependent on the electric field strength and the zeta-potential. This phenomenon can thus be used to determine the zeta-potential of the channel wall by measuring the velocity of the fluid. In this work, another approach to measure the zeta-potential of a confined channel is used. We make use of the so-called streaming potential.

Consider a glass capillary filled with an electrolyte such as in Figure 5 (a). When a linear pressure gradient is applied across the channel the electrolyte will start to flow. This fluid flow results in an ionic convection current (I_s)

by carrying excess counterion ions in the EDL along. A potential will build up at the end of the channel which induces an ionic conduction current (I_c) through the capillary. This conduction current is opposite to the convection current (Figure 5 (a)) [19, 28, 29]. The conduction current can induce a fluid flow due to viscous drag forces in opposite direction to the pressure driven flow. We prove, however, in Appendix C that the opposing flow is negligible, and the resulting velocity profile will be parabolic.

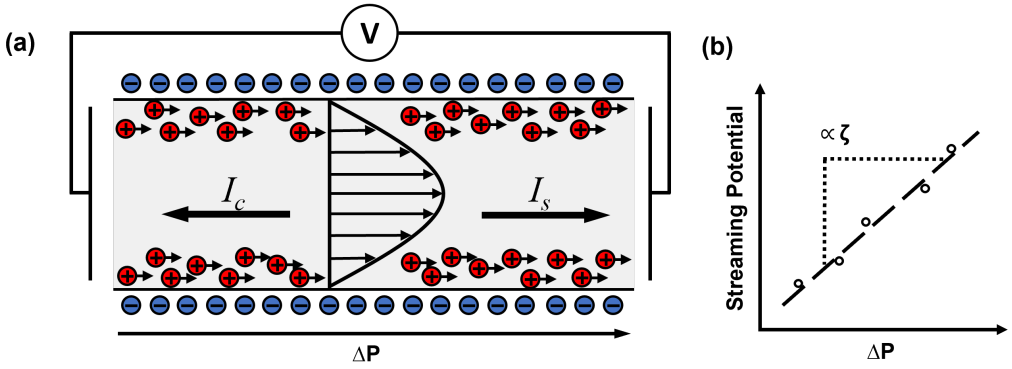

Figure 5: **(a)** Schematic representation of the streaming potential in a channel with a negatively charged wall. A pressure difference is applied from left to right, indicated by the velocity profile. The ionic convection current I_s and the counteracting ionic conduction current I_c are indicated. **(b)** Schematic representation of the streaming potential for different pressure differences ΔP. The zeta-potential follows from the slope of the linear fit.

For the steady-state situation these two currents exactly counterbalance each other. The convective current I_s scales with the pressure and the conductive current I_c with the potential. This gives a proportionality between the applied pressure and developed potential in the steady-state. Equation (7) expresses the potential U_{str} that develops due to an applied pressure difference ΔP, with K_L the conductivity of the solution [19, 26, 30]. This potential is known as the streaming potential and can be determined by measuring the electric potential across the channel using a voltmeter.

$$U_{str} = -\zeta \frac{\epsilon_0 \epsilon_r}{\eta K_L} \Delta P \tag{7}$$

The streaming potential is linearly dependent on the applied pressure difference. When the streaming potential is measured and plotted for different pressures the zeta-potential can be calculated from the slope of a linear fit (Figure 5 (b)). The pressure needs to be controlled, for instance by flowing a liquid through the channel driven by a syringe pump. The applied pressure can then be calculated for a round channel according to the Hagen-Poiseuille equation [31]:

$$\Delta P = \frac{8 \eta L Q}{\pi r^4} \tag{8}$$

With η the viscosity of the liquid, L the length of the channel, Q the volumetric flow rate through the channel, and r the radius of the channel. The above equations are only valid for laminar flow [29]. Laminar flow occurs for Reynolds numbers below approximately 2040 [32]. The Reynolds number (Re) can be calculated for a round channel according to Equation 9 [32–34]. With Re the Reynolds number, ρ the density of the fluid, Q the volumetric flow rate, D the diameter of the channel, η the viscosity of the fluid, and A the diameter of the channel.

$$Re = \frac{\rho Q D}{\eta A} \tag{9}$$

2.1.3 Electrophoresis

Both electroosmosis and streaming potential describe electrokinetic *fluid* transport with respect to a stationary solid phase. In contrast, electrophoresis refers to electrokinetic *mass* transport of a dispersed particle or a solute with respect to a stationary liquid. The movement is driven by an electric field that acts on the charge of the solute.

In the simplest case electrophoresis is the reverse of electroosmosis. The mathematical derivation of section 2.1.1 can be transferred by considering the liquid as stationary and the solid as moving. The velocity of a particle moving in an electric field (v_{EP}) follows the same relation as Equation (6), however, barring the minus sign to indicate the movement of the particle in opposite direction. This relation gives the Smoluchowski's equation, with μ_{EP} the electrophoretic mobility [19, 27, 35].

$$v_{EP} = \frac{\epsilon_0 \epsilon_r \zeta}{\eta} E = \mu_{EP} E \tag{10}$$

Equation (10) can also be derived based on a force balance between the electrostatic Coulomb force acting on the particle and the counteracting friction force the liquid exerts on the particle. Furthermore, an electrophoretic retardation force acts on the particle which stems from the movement of the counterions of the EDL around the particle [19, 27]. These counterions experience the electric field and will move in the opposite direction as the particle. The liquid transported by the movement of these ions works against the motion of the particle (Figure 6) [24, 36, 37]. The magnitude of the electrophoretic retardation force scales with the ionic strength of the electrolyte.

To understand the impact of the ionic strength on the electrophoretic retardation we need to introduce the so-called Debye length κ^{-1}. The Debye length is a property of the EDL that describes the typical length scale over which the EDL extends into the bulk [19, 27, 37]. A large κ^{-1} corresponds to a thick EDL, the diffuse layer extends far into the bulk. A small κ^{-1} corresponds to a thin EDL, the diffuse layer does not extend far into the

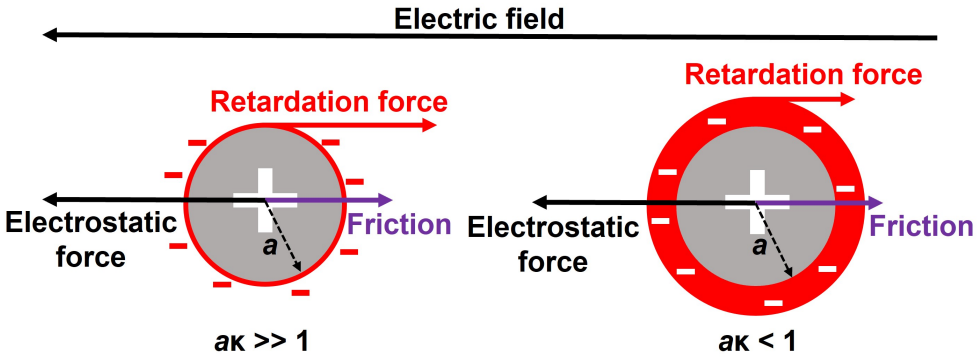

Figure 6: Schematic representation of the forces acting on a positively charged particle in a homogeneous electric field for the case of a thin electric double layer ($a\kappa >> 1$) and the case of a thick electric double layer ($a\kappa < 1$). The thickness of the red circle schematically illustrates the thickness of the electric double layer.

bulk. The Debye length can be calculated according to Equation (11) and is a function of the ionic strength of the solution (Eq. (12)) [19, 27, 37].

$$\kappa^{-1} = \sqrt{\frac{\epsilon_r \epsilon_0 k_B T}{2e^2 I}} \tag{11}$$

$$I = \frac{1}{2} \sum c_i z_i^2 \tag{12}$$

With k_B the Boltzmann constant, T the temperature, e the elementary charge, c_i the molar concentration of ion i, and z_i the charge number of ion i. As follows from Equation (11) a high ionic strength corresponds to a small Debye length and thus, a thin EDL. In turn, a low ionic strength corresponds to a large Debye length and a thick EDL. It is important to note that the thickness of the EDL does not influence the total charge in the EDL. It only indicates how smeared out the charge is into the bulk.

The influence of the ionic strength on the electrophoretic retardation can be explained as follows: at high ionic strength ($a\kappa \gg 1$, with a the particle radius and κ the reciprocal Debye length) the counterions are distributed closely around the particle (Figure 4). The induced fluid flow opposite to the particle movement will be focussed around the particle. As a result, the particle experiences the retardation force strongly. At low ionic strength, however, ($a\kappa < 1$) the counterions will induce a fluid flow less focussed around the particle. In consequence, the total retardation acting on the particle is smaller.

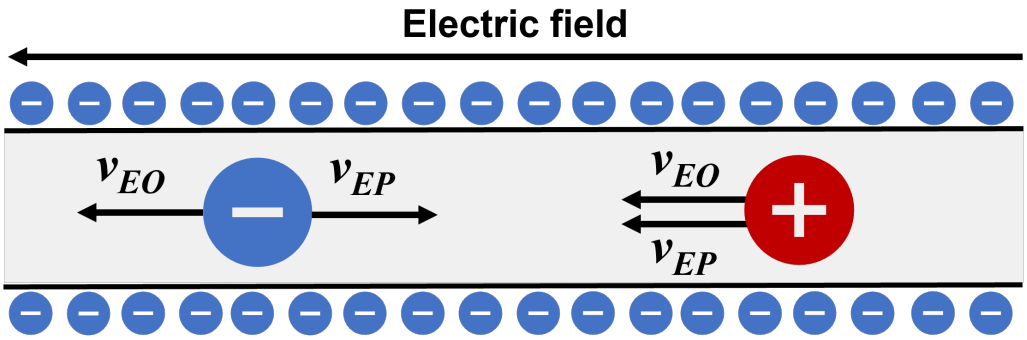

Figure 7: Schematic representation of a negative and positively charged particle in a channel with a negatively charged wall under the influence of an electric field. The negatively charged particle experiences the electroosmotic and electrophoretic velocities in opposing directions. This will result in a lower mobility. The positive particle experiences the electroosmotic and electrophoretic velocities in the same direction. This will result in a higher mobility.

Finally, electrophoresis and electroosmosis often occur simultaneously. Depending on the species' charge and the charge of the confinement these electrokinetic effects can amplify or attenuate each other (Figure 7). This increases or decreases the mobility of the charged species.

2.2 Polyelectrolytes

The purpose of this research is to study the electrokinetic transport of polyelectrolytes (PEs). PEs are polymers for which a large portion of the repeating units contains a charge or chargeable group [9]. PEs can be of anionic (polyanion), cationic (polycation), or zwitterionic charge. PEs have characteristic properties compared to uncharged polymers, such as their excellent water solubility and the strong interaction they form with charged surfaces and other PEs [6, 38].

Here, we will first make the distinction between weak and strong PEs. Next, the adsorption of PEs on charged surfaces and multilayer formation will be discussed.

2.2.1 Weak and strong polyelectrolytes

Many properties of PEs are dependent on the electrostatic interactions they form. As a result the charge density of the polymer chain is an important parameter controlling these properties. A distinction can be made between two different dissociation behaviors of a PE's charged group, describing the PE's charge density behavior.

A weak PE dissociates in response to the pH of the surrounding medium [6, 10, 39, 40]. An example of a weak PE is poly(methacrylic acid) [40]. Its structure and dissociation behavior are given in Figure 8 (a) [41]. Strong PEs are

fully dissociated upon dissolving irrespective of the pH of the surrounding medium [6, 10, 39, 40]. An example of a strong PE is poly(styrene sulfonate) (PSS) (Figure 8 (b)) [40]. The degree of dissociation of PSS would remain at a constant value of 1 across the full pH range.

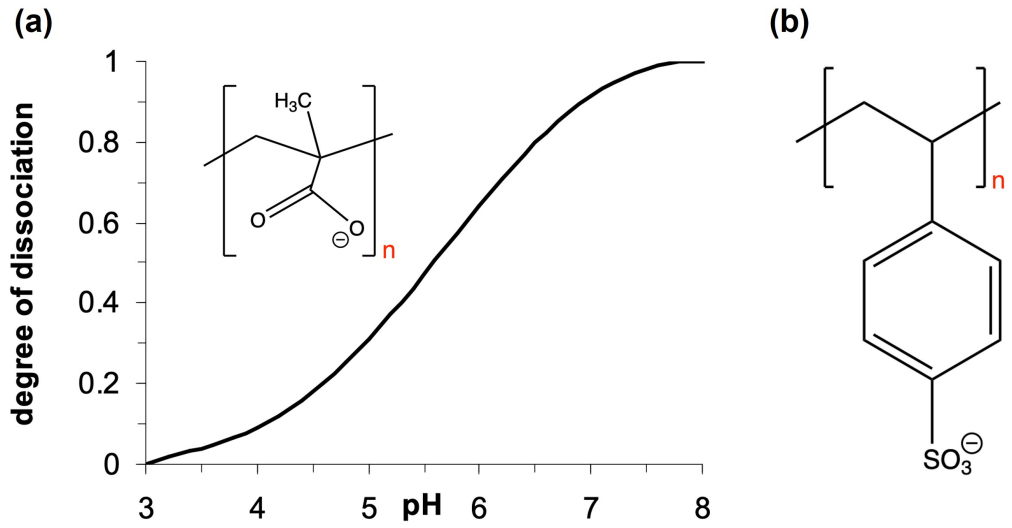

Figure 8: **(a)** Degree of dissociation for the weak PE poly(methacrylic acid) in dependence of pH, adapted from [41]. **(b)** Chemical structure of poly(styrene sulfonate) as example of a strong PE.

2.2.2 Polyelectrolyte adsorption and multilayer formation

PEs preferentially adsorb onto oppositely charged surfaces [42]. The electrostatic interaction between the PE and oppositely charged surface is one of the driving forces that cause the adsorption [6]. The electrostatic interactions are screened by the ionic strength of the solution.

At low ionic strength the PE has an extended conformation in solution due to the many charges along the chain repelling each other (Figure 9 (a) [43–45]). The solution cannot sufficiently compensate or screen these charges for the chain to be flexible. As a result the PE will adsorb in an extended conformation on an oppositely charged surface to compensate as much of its charge (Figure 9 (b)) [42–44, 46, 47].

At higher ionic strengths the PE can form more coiled structures, bringing the repelling charges along its chain closer together (Figure 9 (a)) [43–45, 48]. This is possible because the ions in the solution can screen the repelling charges better. PEs adsorbed at high ionic strength are thus able to form loops away from the surface into the bulk. This creates a thicker PE layer on the surface (Figure 9 (b)) [43, 44, 46, 48]. In this regard, scaling laws proposing the increase of the adsorbed amount of PE (Γ) with the salt concentration

of solution to be $\Gamma \propto \sqrt{c_s}$ have found excellent agreement with experimental studies [49–51].

The stability of adsorbed PE layers is dependent on the type of PE. Strong PE coatings have been shown to be stable for up to twenty hours of continuous rinsing [52–54]. Weak PE coatings, however, degrade significantly upon continuous rinsing already after two hours [52–54].

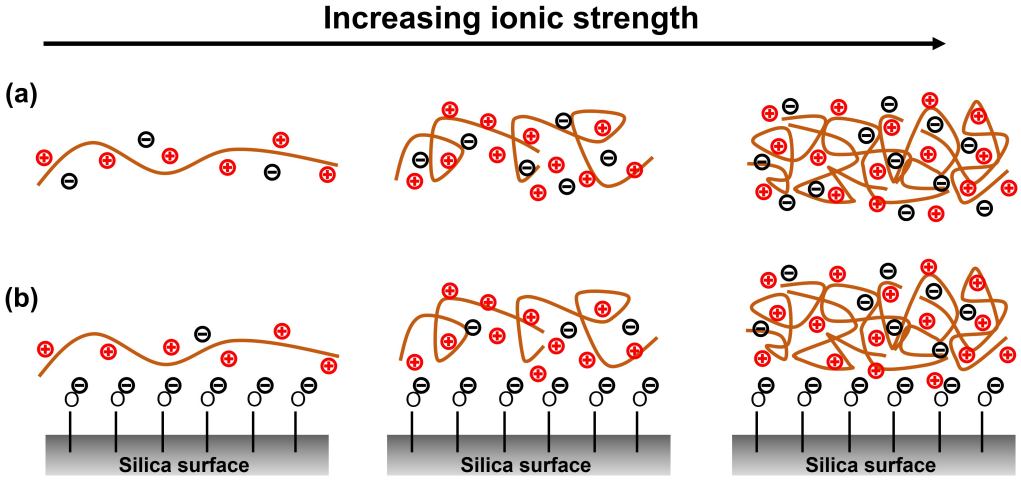

Figure 9: **(a)** Schematic representation of a polycation dissolved in a solution of increasing ionic strength. **(b)** Schematic representation of a polycation adsorbed on a silica surface for varying ionic strength of the bulk solution.

However, electrostatics do not explain the full adsorption behavior of PEs on charged surfaces. Entropy has been shown to play a crucial role in the adsorption behavior of PEs [6, 42, 43, 55]. The release of counterions from the surface and the PE can result in entropic gain that drives the PE adsorption. On the other hand, the loss of conformational freedom of the PE upon adsorption can introduce an entropic penalty.

Furthermore, other non-electrostatic interactions between the PE and the surface are present. This can be concluded from the observation of charge overcompensation [42, 43, 47, 55]. Charge overcompensation describes the adsorption of PEs on a surface beyond the point of electroneutrality [46]. This results in a new charged surface of opposite sign. If electrostatic interactions would be dominating, charge overcompensation would not occur.

Charge overcompensation is also an essential driving force in the formation of PE multilayers (PEMs) [56]. PEMs are formed by sequential adsorption of a polycation and a polyanion onto a charged surface [6, 57, 58]. PEMs can be used as thin and selective separation membranes [57, 59, 60].

2.3 Static light scattering

The coiling of a PE in dependence of the ionic strength can be studied by measuring the radius of gyration (R_g) of the PE. R_g gives the distance from the center of mass of the polymer at which the entire mass can be assumed to be concentrated [61]. It is thus a measure of the size of the polymer and depends *e.g.* on the molecular weight of the polymer and the type of solvent [61, 62]. Static light scattering (SLS) can be used to determine R_g of a polymer [63]. In SLS experiments the time-averaged intensity of scattered light from a sample is measured as a function of the scattering angle [64]. R_g can be determined from SLS data according to the Guinier approximation (Eq. (13)) [62, 65, 66].

$$I(q) \simeq I(0)e^{-q^2 R_g^2/3} \tag{13}$$

$$q = \frac{4\pi}{\lambda} \sin\theta \tag{14}$$

With $I(q)$ the scattering intensity, $I(0)$ the forward scattering intensity, and q the scattering vector given by Equation (14), with λ the wavelength of the incident light, and θ the scattering angle. From Equation (13) it can be deduced that plotting $\ln I(q)$ as a function of q^2 gives R_g as the slope of a linear fit.

3 Materials and methods

This chapter provides an overview of the chemicals and materials used and gives a detailed description of all experimental procedures.

3.1 Chemicals, materials, and equipment

Table 1: Overview of all chemicals used, their CAS-numbers, and the suppliers.

Name	CAS-number	Supplier
Fluorescein sodium salt (fluorescent tracer)	518–47–8	Sigma-Aldrich
Poly(fluorescein isothiocyanate allylamine hydrochloride) (PAH-FITC) (MW 56 kDa)	71550–12–4	Aldridge
poly(diallyldimethylammonium chloride) (pDADMAC) (MW <100 kDa, 35 wt % in water)	26062–79–3	Sigma-Aldrich
poly(diallyldimethylammonium chloride) (pDADMAC) (MW 200–350 kDa, 20 wt % in water)	26062–79–3	Aldrich chemistry
poly(diallyldimethylammonium chloride) (pDADMAC) (MW 400–500 kDa, 20 wt % in water)	26062–79–3	Aldrich chemistry
Rhodamine B ($\geqslant$ 95.0 %*)	81–88–9	Sigma life sciences
Sodium Chloride ($\geqslant$ 99.5 %*)	7647–14–5	Sigma-Aldrich
Sodium phosphate dibasic ($\geqslant$ 99.0 %*)	7558–79–4	Sigma-Aldrich
Sodium phosphate mononbasic dihydrate ($\geqslant$ 99.0 %*)	13472–35–0	Sigma life sciences
Water (18.2 MΩcm)	7732–18–5	Synergy Millipore

*) Purity

Table 2: Overview of the analytical equipment used.

Description	Specification	Supplier
Bright/dark field microscope	M205C, Plan 0.5x M-series objective	Leica Microsystems
Confocal laser scanning microscope	Stellaris 5	Leica Microsystems
Syringe pump	Legato 100	kd Scientific
Multimeter	UT161D, including software	Uni-T
DC power supply	ES0300-0.45	Delta Elektronika
pH meter	pH 210 Microprocessor pH meter	Hanna Instruments
pH probe	InLab Expert Pro	Mettler Toledo
Conductivity meter	SevenExcellence Multiparameter	Mettler Toledo
Conductivity probe	InLab 731-ISM	Mettler Toledo
Static light scattering	Home-built setup	-

Table 3: Overview of materials used.

Description	Specification	Supplier
Round boro capillary	50 μm inner diamter, length 10 cm	VitroCom
Square boro capillary	200×200 μm, length 10 cm	VitroCom
Rectangular boro capillary	100×2000 μm, length 5 cm	VitroCom
Rectangular boro capillary	100×2000 μm, length 10 cm	VitroCom
Microscope slide	ISO 8031/1, 76×26 mm	Epredia
Tubing	20 gauge thin wall PTFE	Cole Parmer
Syringe	Injekt Luer Solo 2 mL	B Braun
Syringe needle	20 gauge, 0.5 inch	Metcal
Syringe filter	16592-K Minisart 0.8 μm pore size	Sartorius
Septum	Precision Seal rubber septum, 19/22 joint	Sigma-Aldrich
T-junction	PEEK Tee 0.020 inch inner diameter	Upchurch Scientific
Fingertight fitting	PEEK fingertight fitting 0.0625 inch inner diameter	Upchurch Scientific
Epoxy glue	6183 Epoxy-Kleber	Liqui Moly
UV glue	NOA81	Norland
PAP pen (mixture of 1-bromopropane and ligroin)	Hydrophobic coatings on glass	Sigma-Aldrich

3.2 Buffer preparation

A 100 mM phosphate buffer was prepared at pH ±8 by mixing 9.32 mL of a 1 M Na_2HPO_4 solution with 0.68 mL of 1 M NaH_2PO_4 solution, followed by dilution to 100 mL with MilliQ water. The final pH of the buffer could be fine-tuned by addition of 0.2 M HCl or 0.2 M NaOH to pH 7.95.

3.3 pDADMAC capillary coating

$20 - 35$ wt % poly(diallyldimethylammonium chloride) (pDADMAC) stock solutions were diluted to 0.2 wt % with a 20 mM phosphate buffer solution (Section 3.2). Coating solutions were prepared by adding 0, 50, 250, 500, and 750 mM NaCl to 0.2 wt % pDADMAC solutions. Round or rectangular capillaries were placed upright in a vial containing the coating solution and filled through capillary forces. After 5 minutes the capillary was flushed with an electrolyte solution four times. The electrolyte solution used was dependent on the experiment for which the capillary was used.

3.4 Zeta-potential measurements

The zeta-potential of the inner wall of pDADMAC coated and uncoated capillaries was determined using the streaming potential as described in Section 2.1.2. To measure the streaming potential a custom setup was built (Figure 10). A photograph showing the zeta-potential setup is given in Appendix A (Figure 33)

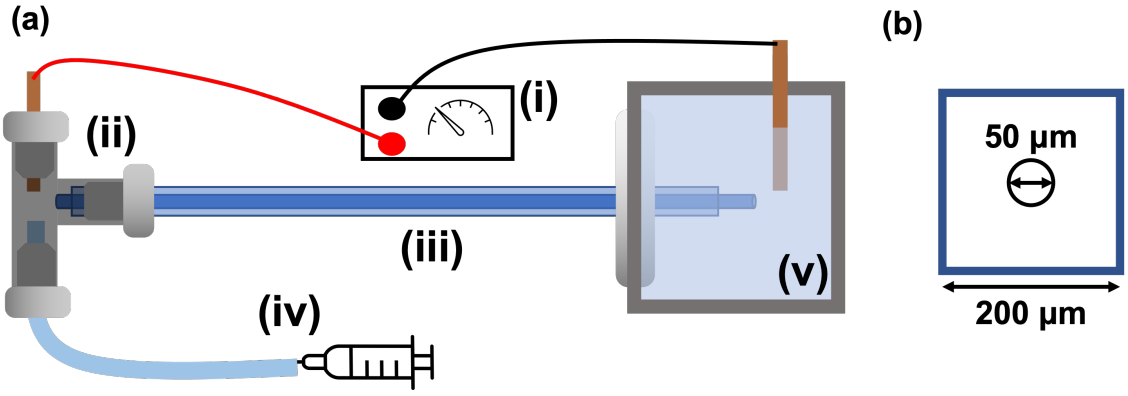

Figure 10: **(a)** Schematic representation of the setup used to measure the streaming potential of the inner wall of a round capillary. (*i*) Voltmeter connected to two copper electrodes; (*ii*) T-junction with fingertight fittings to connect tubing, a copper electrode, and a capillary; (*iii*) 50 μm inner diameter round capillary glued into a 200 μm square capillary for support; (*iv*) Syringe pump controlling the pressure by varying the flow rate of the electrolyte; (*v*) Reservoir filled with the running electrolyte and sealed using a septum. **(b)** Schematic showing to alignment of the two capillaries that are glued together.

A round capillary with 50 μm inner diameter (ID) was glued into a 200 μm square capillary for reinforcement using UV glue (Figure 10 (b)). The ends of the round inner capillary were left open. The square outer capillary was closed off with UV-glue, so flow could only occur through the inner capillary. Next, these capillaries were glued into a fingertight fitting using epoxy glue. The fitting was screwed into a T-junction, which allowed the capillary to be connected leak-free to tubing and a copper electrode. The copper electrode was glued into a fingertight fitting, sticking out on both sides, and screwed into the T-junction. The tubing was pulled through a fingertight fitting, which was screwed into the T-junction. The other end of the tubing was connected to a 2 mL syringe containing a 2 mM phosphate buffer solution (K_L = 44 mS/m). The syringe was connected to a syringe pump to apply a pressure. Flow rates were kept low to ensure laminar flow. The capillary was inserted through a septum into a 3D printed reservoir containing the 2 mM phosphate buffer solution. Finally, a voltmeter was connected to the T-junction copper electrode, and a copper electrode inserted into the reservoir.

The voltmeter logged the measured potential across the capillary every

second on a computer. Before and after the syringe pump was turned on the system was left to equilibrate to a constant potential. The streaming potential U_{str} was calculated as the difference between the equilibrated potential before and after applying a pressure difference across the capillary (Figure 11). Plotting the streaming potential as a function of the applied pressure allowed to calculate the zeta-potential from the slope of the linear fit (Eq. (7)).

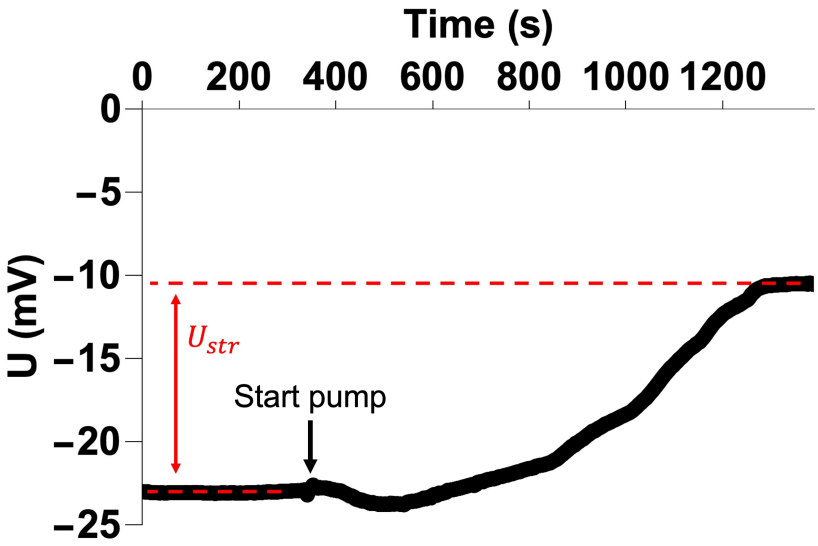

Figure 11: Representative data of a streaming potential measurement. The streaming potential is calculated as the difference between the equilibrated potential before and after applying a pressure.

3.5 Capillary cell setup

To measure electroosmotic and electrophoretic mobilities, a capillary cell was built. On a glass microscope slide a 5 cm long 2 × 0.1 mm ID rectangular capillary was glued using epoxy glue (Figure 12 (a)). At either opening of the capillary a reservoir was built for droplets of the buffer solution. Using epoxy glue a barrier was made over the capillary to eliminate capillary forces pulling the liquid underneath the capillary. The other three sides of the reservoir were given a hydrophobic coating using a PAP pen to contain the droplet. The glass slide was placed into a 3D printed container which was open on the top and had supports on the bottom. To hold two copper electrodes in place a 3D printed frame that fitted over the 3D printed container was fabricated (Figures 12 (b, c)). The electrodes were inserted through the side of the frame and bent down to reach into the reservoirs. The electrodes were kept in place with two screws.

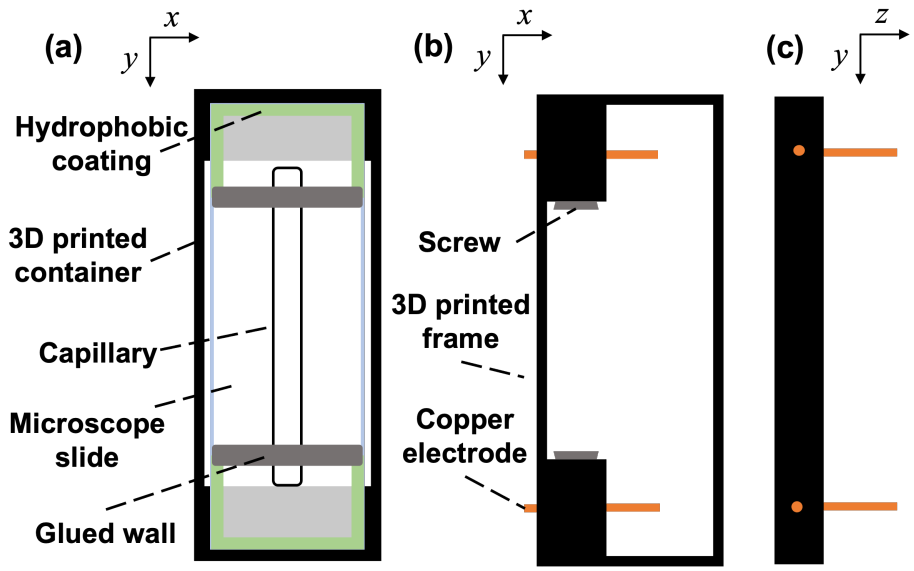

Figure 12: Schematic showing the capillary cell. **(a)** Top view of the glass slide and 3D printed container. **(b)** Top view of the electrode holder. **(c)** Side view of the electrode holder.

This cell setup can furthermore be extended to increase the length over which electroosmotic or electrophoretic migration is observed. To this end, two glass slides could be glued together to account for a longer capillary and the 3D printed parts were redesigned accordingly.

3.6 Electroosmotic mobility measurements

A 5 mg/mL rhodamine B solution containing 20 mM phosphate buffer and 30 mM NaCl was prepared at pH 7.95. Rhodamine B was used as a neutral marker. Rhodamine B carries a carboxylic acid group with a pKa value of 3.2 [67]. The deprotonated form of rhodamine B is in tautomeric equilibrium between a zwitterionic and a neutral state (Figure 13) [67]. Both the neutral and zwitterionic state of rhodamine B cannot migrate electrophoretically. By performing the measurements at pH 7.95 it is thus ensured that the migration of rhodamine B is only due to electroosmotic flow.

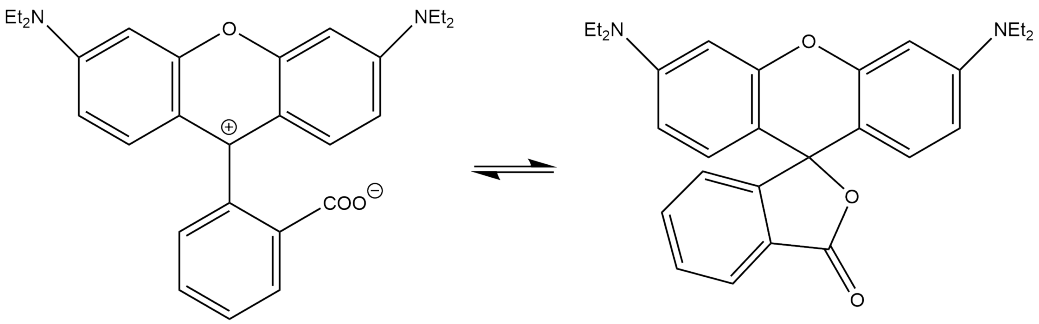

Figure 13: Tautomeric equilibrium of deprotonated rhodamine B, adapted from [67].

The capillary cell was placed under the bright field microscope and the electrodes were connected to a DC power supply. A voltmeter was used to read out the applied electric field (Figure 14, see Appendix A Figure 34 for a photograph of the setup). The two reservoirs were filled with 300 µL of phosphate buffer, containing additional 30 mM NaCl to increase the conductivity. The system was left to equilibrate for 10–15 minutes to eliminate gravity induced flow. Next, the power supply was turned on, and the system was left to equilibrate for further 10–15 minutes at 1900 V/m (Applied voltage: 100 V). The power supply was turned off and 50 µL was pipetted out of each reservoir and replaced with 50 µL of the rhodamine B containing solution resulting in a final rhodamine B concentration of 0.83 mg/mL. The power supply was turned on again and the measurement was started (E = 1900 V/m). Images were acquired every 10–15 seconds.

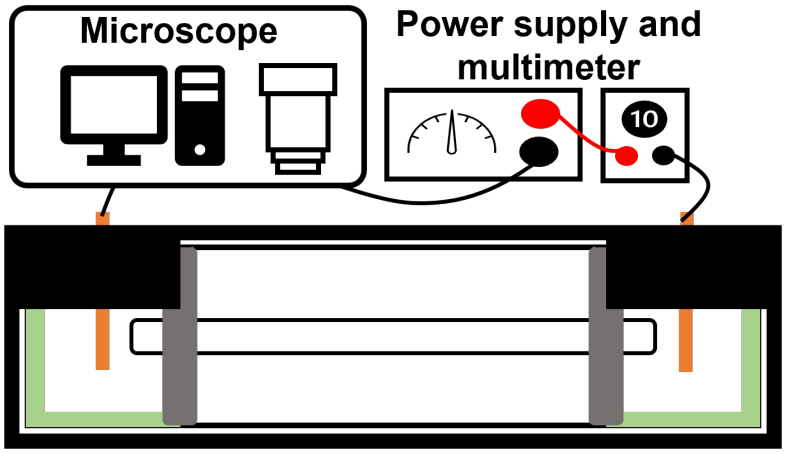

Figure 14: Schematic showing the capillary cell setup used during measurement of the electroosmotic flow through the capillary.

3.7 Data-analysis

Microscope images were exported to ImageJ and analyzed to extract the mobility (Figure 15). The mean gray value (MGV) of a line extending over the width of the capillary was measured for every image. This was done for three lines separated by a distance Δx (Figure 15 (a)). The MGV was normalized and plotted over time for the three different positions (Figure 15 (b)). To calculate the migration time over a distance Δx the time differences Δt were computed. Δt was defined as the time needed to achieve the same MGV between two positions separated by a distance Δx (Figure 15 (b)). These time differences were typically calculated for 10–50 normalized MGVs. From the known spacing Δx and the calculated Δt, velocities v can be calculated. Velocities were determined not only for the single spacing (Δx and Δt), but also for double-spacing ($2\Delta x$ and $2\Delta t$). The velocities were averaged, and the mobility could be calculated using Equation (15) and the applied electric field E.

$$\mu = \frac{v}{E} = \frac{\Delta x}{\Delta t}\frac{1}{E} \tag{15}$$

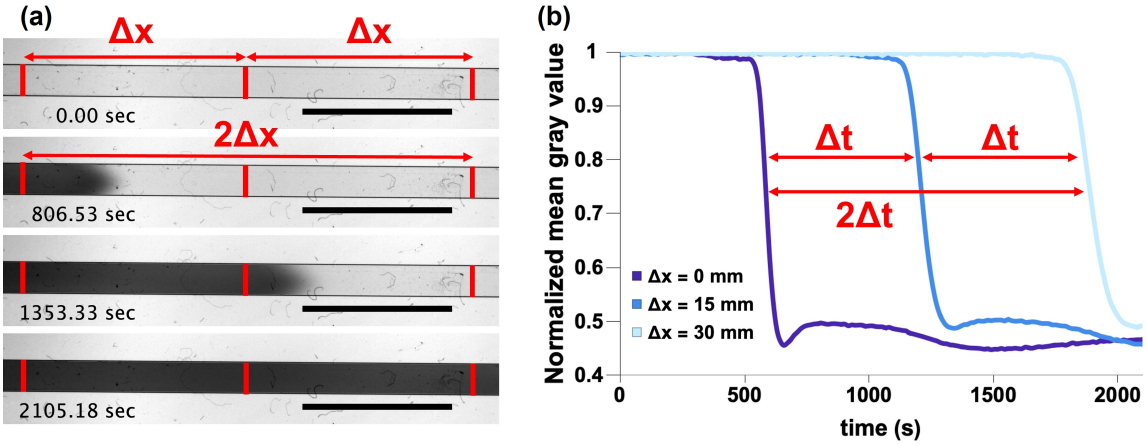

Figure 15: **(a)** Microscopy images from measuring the electroosmotic mobility. Indicated are the positions for the mean gray value (MGV) measurements and the spacing between them (Δx). The scale bars are 10 mm. **(b)** A plot of the normalized mean gray value for the measurement shown in **(a)**. Indicated are the time differences (Δt) for each position to reach a certain MGV.

3.8 Electroosmotic flow simulations

A 2D COMSOL Multiphysics model with the physics module *Transport of Dilute Species* was designed to simulate the electroosmotic flow through a capillary. A channel geometry was created by a rectangle of 0.1 mm width

and 33 mm length (Figure 16 (a)). A physics-controlled coarse mesh was used. The top and bottom walls of the rectangle were assigned an electroosmotic flow boundary condition with the zeta-potential as experimental parameter. An electric field was set parallel to the top and bottom wall with a magnitude of 1900 V/m. The right wall of the channel was given an open boundary condition to allow outflow. The left wall was modelled as reservoir containing a neutral molecule (*Sp.*1) representing rhodamine B. *Sp.*1 was allowed to be transported by convection and diffusion. The concentration of *Sp.*1 in the reservoir was set to 1 M and the diffusion coefficient was set to 4.5×10^{-10} $m^2\,s^{-1}$, corresponding to the diffusion coefficient of rhodamine B [68].

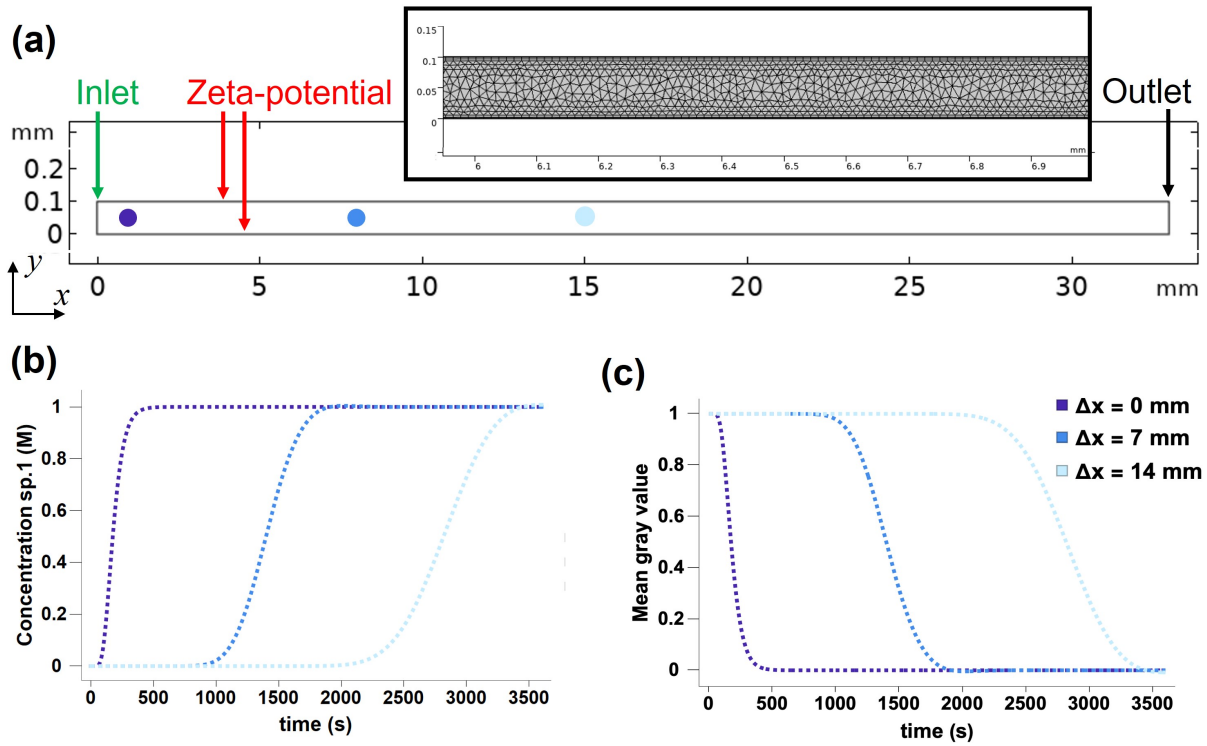

Figure 16: **(a)** Channel geometry of the COMSOL model. The blue dots indicate the points where the concentration of *Sp.*1 was measured. The simulation was performed using a physics-controlled coarse mesh shown in the inset of (a). **(b)** Plot showing the change in concentration of *Sp.*1 at the blue points in (a). Legend is the same as given in (c). **(c)** Plot showing the mean gray value as a function of time for the blue points given in (a). The lines were calculated by performing $y_{MGV} = -y_{conc} + 1$ on the data in (b).

A time-dependent simulation shows the migration of the neutral marker due to electroosmotic flow. The electroosmotic mobility was calculated from the model for a given zeta-potential by measuring the concentration of *Sp.*1 at three different position along the length of the channel Figure 16 (b). The concentration values were converted to MGV by performing $y_{MGV} =$

$-y_{conc}+1$ for each value of y_{conc} (Figure 16 (c)). Based on this, MGV analysis as described in the previous section is used to calculate the electroosmotic mobility.

3.9 Electrophoretic mobility measurements

3.9.1 Fluorescein

To measure the electrophoretic mobility of fluorescein (FL) the same setup and procedure was used as in Section 3.6. A stock solution of 10 mg/mL FL in 20 mM phosphate buffer of pH 7.95 with 30 mM NaCl was prepared. 300 μL of 20 mM phosphate buffer solution with 30 mM NaCl was pipetted into both reservoirs of the capillary cell setup. The system was left to equilibrate for 10–15 minutes to eliminate gravity induced flow. Next, an electric field of 1900 V/m was applied for 10–15 minutes. The electric field was turned off and 100 µL of the phosphate buffer in the reservoirs was replaced with 100 µL of the FL solution. The electric field was turned on again and the measurement was started.

Data analysis was performed via MGV analysis as described in Section 3.7.

3.9.2 PAH-FITC

Electrophoretic mobility measurements of poly(fluorescein isothiocyanate allylamine hydrochloride) (PAH-FITC) were performed using the setup and procedure described in section 3.6. A stock solution of 0.5 mg/mL PAH-FITC in water was prepared at pH 4.2. Measurements were performed in dark field mode under the microscope using fluorescence to track the migration of PAH-FITC in the electric field. A 405 nm laser pen was used to excite PAH-FITC. As running electrolyte an 80 mM NaCl solution at pH 4.2±0.05 was used. The system was equilibrated for the electric field of 1900 V/m. Next, 100 µL of the NaCl solution in the reservoirs was replaced with 100 µL of the PAH-FITC solution and the measurement was started.

Data analysis was performed via MGV analysis as described in Section 3.7.

3.10 UV/Vis spectroscopy

The fluorescence spectrum of PAH-FITC was recorded using a confocal laser scanning microscope. Droplets of 0.5 mg/mL PAH-FITC solution were placed on a glass slide under the microscope. Spectra were recorded by performing a λ-scan in the range $490 - 590$ nm with a step size of 3 nm and excitation wavelength of 488 nm. The z-position of the microscope was kept constant in the center of the droplet for each measurement.

3.11 SLS of pDADMAC

Static light scattering (SLS) was employed to measure the radius of gyration (R_g) of pDADMAC. A custom build SLS setup was used consisting of a mercury-vapor lamp, optical system, sample holder, and detector (Figure 17). The optical system includes: filters to regulate the light intensity, color, and polarization, a slit, and a lens system that focuses the light on the sample. The sample holder fitted a round glass cuvette. As detector a photomultiplier tube mounted on a rotating arm was used to measure the scattered light at different angles.

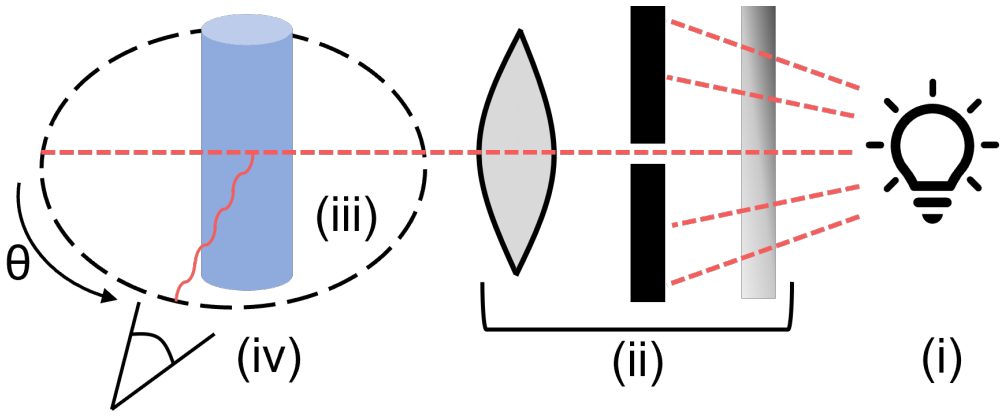

Figure 17: Schematic representation of the SLS setup used to measure the radius of gyration of pDADMAC. The dotted red line indicates the emitted light from the mercury-vapor lamp. The undulating line indicates the scattered light at angle θ. (*i*) Mercury-vapor lamp; (*ii*) Optical system including intensity, color, and polarization filters, a slit, and lenses; (*iii*) Sample holder with a round glass cuvette; (*iv*) Photomultiplier tube mounted on a rotating arm.

pDADMAC (MW 200–350 kDa) was diluted to 0.2 wt % using NaCl, and phosphate buffer solutions of ionic strength 1 mM, 10 mM, 50 mM, 100 mM, 500 mM, and 1 M respectively. The samples were filtered through a syringe filter (0.8 μm pore size) into the round glass cuvette. The scattered light intensity was measured for 41 angles evenly spaced between $\theta = 20°$ and $\theta = 140°$ using light with a wavelength of 578 nm. At every angle the intensity was averaged over 3 seconds. From the slope of a Guinier plot R_g was determined.

4 Results and discussion

In this chapter the findings of this thesis will be discussed. Control of the electroosmotic flow through the capillary cell is achieved by applying a pDADMAC coating. The influence of the pDADMAC chain length and the divalent phosphate buffer on the pDADMAC adsorption were investigated. Electrophoretic mobility (μ_{EP}) measurements were validated by measuring μ_{EP} of fluorescein and comparing this to literature values. Finally, μ_{EP} was determined for poly(allylamine hydrochloride) as model PE.

4.1 Electroosmotic flow suppression

To allow accurate measurement of electrophoretic mobilities we aimed to eliminate electroosmotic flow (EOF) through the glass capillaries. To suppress EOF through capillaries, the inner glass surface was coated with high MW pDADMAC (MW 400–500 kDa). The coating was performed for different NaCl concentrations. The electroosmotic mobility μ_{EO} was measured for each coating (Figure 18). The influence of any pressure driven flow is excluded by examining the velocity profile of the flow, see Appendix B.

For the uncoated capillary an electroosmotic mobility of $\mu_{EO} = 36 \times 10^{-9}$ $m^2\,V^{-1}\,s^{-1}$ was determined. This corresponds well to literature values [69]. The pDADMAC coated capillaries showed a reverse in the sign of μ_{EO} indicating a flow in opposite direction to the uncoated case. Furthermore, the absolute value of μ_{EO} decreases with increasing NaCl concentration during the coating.

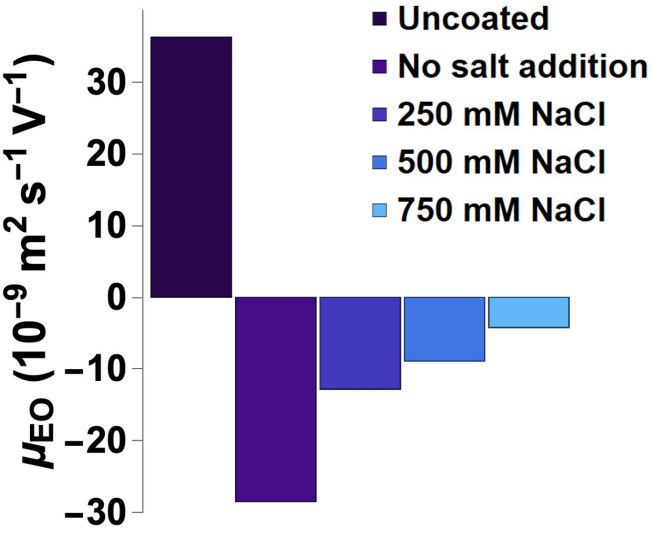

Figure 18: The electroosmotic mobility (μ_{EO}) for an uncoated capillary and capillaries coated with high MW pDADMAC at different NaCl concentrations.

As the electroosmotic mobility is directly dependent on the zeta-potential (Eq. (6)), the values of μ_{EO} can be validated by measurement of the zeta-potential of the coated capillaries using the streaming potential (U_{str}) (Figure 19 (a)).

The streaming potential was averaged over three measurements for each pressure. The standard deviation for each data point was calculated. The standard deviation was then given as a weight for each data point to calculate the linear fit according to Equation (7). The weights were defined as $1/error^2$ [70, 71]. This means that data points with a small error contribute more to the determination of the linear fit. This also allows to calculate the error in the slope of the fit.

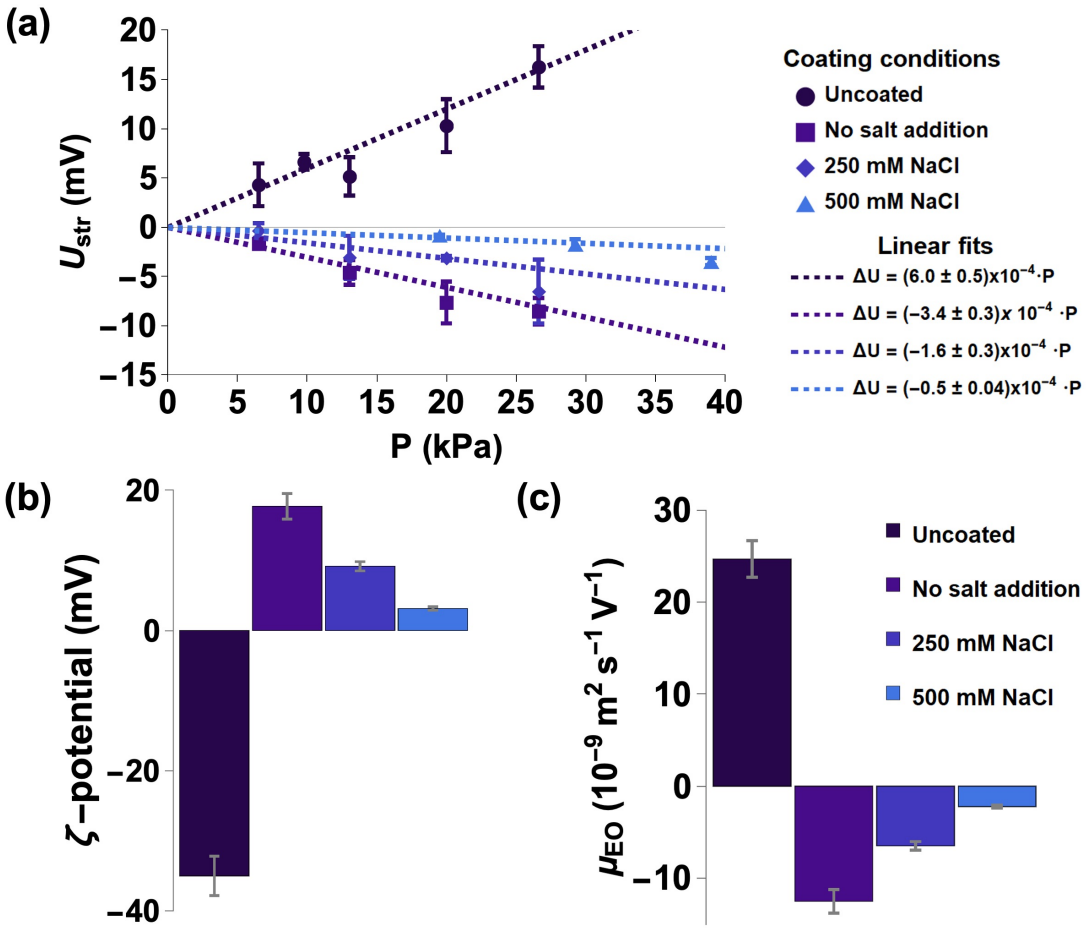

Figure 19: **(a)** Measurement of the streaming potential (U_{str}) as a function of the pressure (P) for an uncoated capillary and capillaries coated with high MW pDADMAC (MW 400–500 kDa) at different NaCl concentrations. The error bars indicate the standard deviation of the measurements. The dashed lines are linear fits based on Equation (7). The measurement errors were used as weights to determine the linear fit. **(b)** Zeta-potentials calculated from the slopes of the linear fits given in (a). **(c)** μ_{EO} calculated from the zeta-potentials in (a). The legend for (b) and (c) are the same and given in (c)

From the linear fits (Figure 19 (a)) the zeta-potential was calculated using Equation (7) (Figure 19 (b)). The zeta-potential of the uncoated capillary was found to be −35 mV. This corresponds well the zeta-potential of fused-silica in a sodium phosphate buffer found in literature ($\zeta = -40$ mV) [72]. Next, μ_{EO} was calculated from the found zeta-potentials using Equation (6) (Figure 19 (c)).

A decrease in the absolute value of μ_{EO} is observed for increasing NaCl concentration in the pDADMAC coating procedure. This trend is observed both from analyzing the EOF, and from streaming potential measurements (Figure 20). This trend, however, is contrary to what is expected from theoretical and experimental data of PE adsorption in literature. The adsorbed amount of PE is generally expected to increase with ionic strength (Section 2.2.2). This would correspond to an increase in charge overcompensation at higher ionic strength, and in a higher zeta-potential and μ_{EO}. Wang *et al.* investigated the electroosmotic flow through pDADMAC coated capillaries (MW 428 kDa) and found an increase of μ_{EO} for coatings at higher ionic strength [69]. Rehmet *et al.* also report an increase in zeta-potential and adsorbed mass of pDADMAC at higher NaCl concentrations during the coating of latex particles [73]. Why do we observe a decrease in the zeta-potential and absolute value of the electrophoretic mobility for coatings at higher salt concentration?

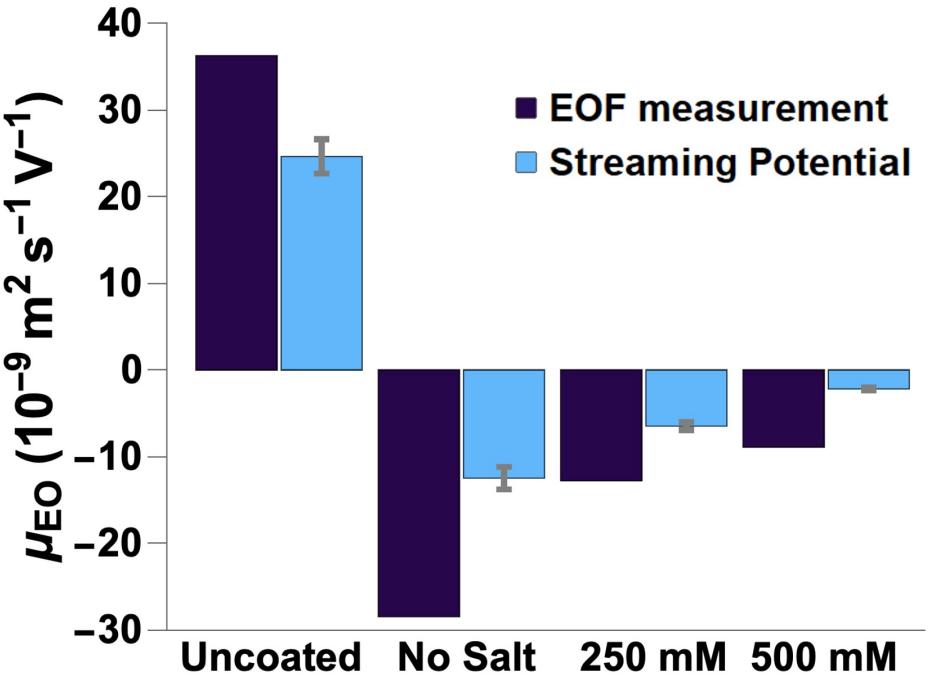

Figure 20: Comparison of values for μ_{EO} capillaries coated with high MW pDADMAC based on the experimental determination of the EOF and streaming potential measurements.

4.1.1 Effect of pDADMAC chain length

Our first hypothesis was that a high MW could affect the pDADMAC adsorption due to steric hindrance, which blocks adsorption sites. To investigate the effect of pDADMAC chain length on the suppression of EOF, μ_{EO} is determined for capillaries coated with low MW pDADMAC (MW $<$ 100 kDa) at different NaCl concentrations by analyzing the EOF (Figure 21 (a)). The measurements were validated by streaming potential measurements to determine the zeta-potential of the capillaries. From the zeta-potential μ_{EO} was calculated using Equation (6) (Figure 21 (b)).

μ_{EO} was lower for almost all coating conditions compared to the high MW pDADMAC coatings. However, a decrease in absolute value of μ_{EO} is still observed for pDADMAC coatings performed at higher salt concentrations from both EOF analysis and streaming potential measurements. The electroosmotic mobility thus decreases with increasing NaCl concentration for both low and high MW pDADMAC coatings. In consequence, the MW of pDADMAC cannot explain the trend of decreasing μ_{EO} with increasing ionic strength during the coating procedure.

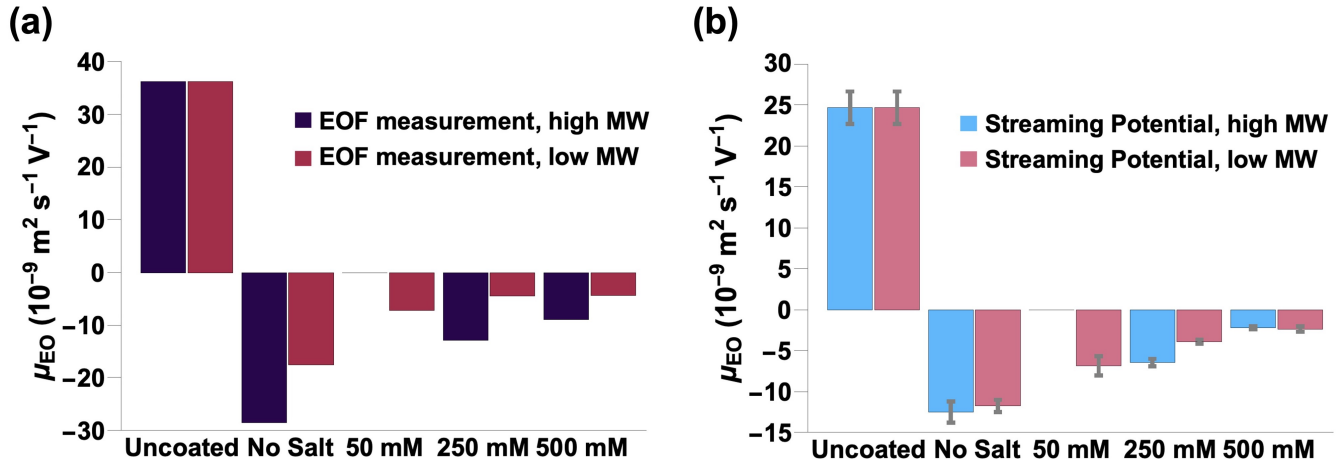

Figure 21: **(a)** μ_{EO} for high and low MW pDADMAC coated capillaries from EOF analysis. **(b)** μ_{EO} for high and low MW pDADMAC coated capillaries from streaming potential measurements.

4.1.2 Effect of phosphate buffer

Next, it was hypothesized that the use of the phosphate buffer during measurements could influence the coiling of the adsorbed chain as the phosphate ion is present as a divalent species (HPO_4^{2-}). It can easily be calculated that at pH 7.95 most of the phosphate ions are present in as HPO_4^{2-}. Phosphate has three pKa values: 2.14, 7.20, and 12.34 [72,74,75]. At pH 7.95, which was

used for the coating experiments, the relevant pKa is 7.20 and the chemical equilibrium is given by Equation (16).

$$H_2PO_4^- \rightleftharpoons H^+ + HPO_4^{2-} \tag{16}$$

The percentage of ions present as HPO_4^{2-} can be calculated from the definition of the pKa (Eq. (17) [76]) to be 85.5%. With the concentration of H^+ predicted by Equation (18) [76].

$$pKa = \frac{[H_2PO_4^-]}{[HPO_4^{2-}][H^+]} \tag{17}$$

$$[H^+] = 10^{-pH} \tag{18}$$

To probe the effect of divalent counterions on the EOF through pDADMAC (MW 200–350 kDa) coated capillaries, streaming potential measurements were performed with pDADMAC coated capillaries using a 2 mM NaCl solution (Figure 22 (a)). The resulting zeta-potentials were used to calculate values of μ_{EO} with Equation (6) (Figure 22 (b)).

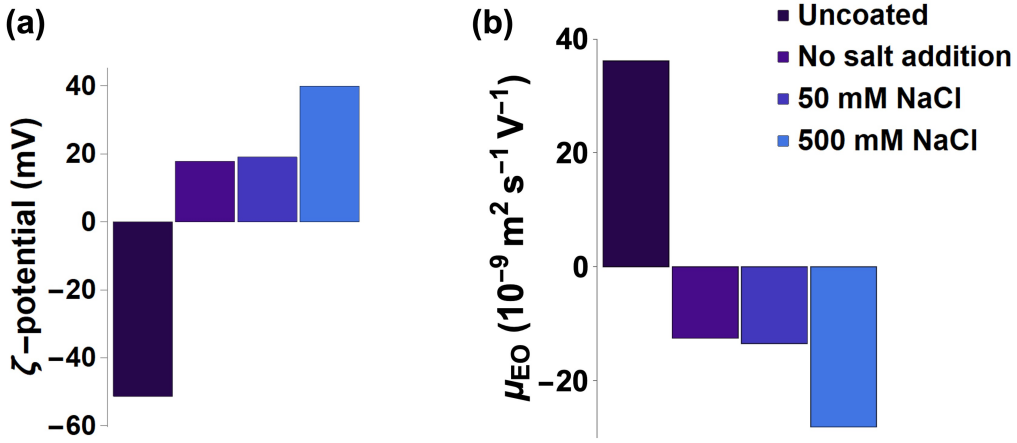

Figure 22: **(a)** Zeta-potentials of uncoated and pDADMAC coated capillaries measured with a 2 mM NaCl solution. **(b)** μ_{EO} as calculated from the zeta-potentials in (a). The legend for **(a)** and **(b)** are the same and given in **(b)**.

The zeta-potential of the uncoated capillary deviates significantly from the value found using the phosphate buffer ($\zeta = -35$ mV, Figure 19 (b)). This can be explained by the lower ionic strength of the 2 mM NaCl solution as compared to the 2 mM phosphate solution. Figure 22 (b) shows that μ_{EO} increases with increasing ionic strength in the absence of divalent counterions as suggested in literature [69,73]. This implies that the presence of a divalent counterion affects the observed EOF of pDADMAC coated capillaries.

Wei *et al.* showed that PE multilayers (PEMs) show a rapid and reversible conformational rearrangement upon exposure to divalent counterions [77]. They argue that divalent ions displace the monovalent counterions

in the PEM driven by entropy. The divalent ions, in consequence, facilitate long-lived attractions between segments of the PE chains. It was shown that this reduces the thickness of the PEM and even neutralizes the charge of the PE chains. We propose here that the divalent HPO_4^{2-} is able to induce a conformational rearrangement of the adsorbed pDADMAC layer, reducing the zeta-potential. This effect would be more pronounced at high salt concentrations which favor the pDADMAC layer to adsorb with loops onto the surface, as these loops are able to change their conformation more freely (Figure 23).

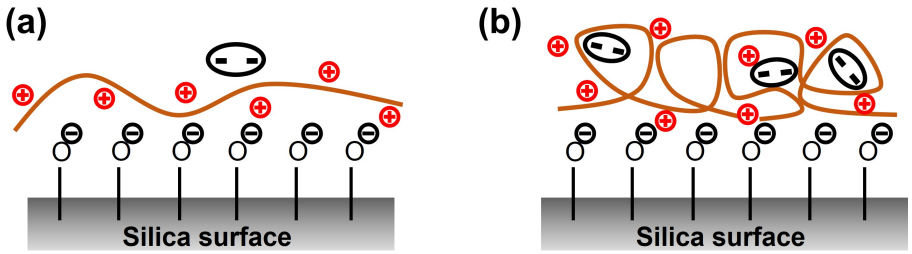

Figure 23: **(a)** Schematic representation of a pDADMAC chain adsorbed on a charged surface at low salt concentration. Conformational rearrangement of loops is not possible as the adsorbed pDADMAC adopts an extended conformation at low salt concentrations. **(b)** Schematic representation of a pDADMAC chain adsorbed on a charged surface at high salt concentration. Loops are able to change their conformation by introducing divalent counterions into the loops.

4.1.3 Conformation of pDADMAC in solution

To probe the effect of divalent counterions on the conformation of adsorbed pDADMAC we investigate the conformation of pDADMAC in an aqueous solution in the presence of divalent counterions using Static light scattering (SLS). The radius of gyration (R_g) was calculated from SLS measurements using the Guinier approximation (Eq. (13)). This was done for pDADMAC in NaCl and phosphate buffer solutions of different ionic strength (Figure 24).

R_g of pDADMAC is smaller for a divalent HPO_4^{2-} counterion compared to the monovalent chloride at every measured ionic strength between 0.01 M and 1 M. From this it was concluded that the divalent HPO_4^{2-} can induce a conformational change of pDADMAC, allowing the pDADMAC to coil more at constant ionic strength. This finding is supported by molecular dynamics simulations of PE chains showing a decrease in R_g for increasing valency of counterions [78].

However, the values for R_g presented here are much higher than found in literature for pDADMAC of similar MW ($R_g \approx 20 - 45$ nm) [79]. This indicates that the determined R_g values were likely dominated by larger clusters of pDADMAC chains, as the scattering intensity of light scales with the radius of a particle to the sixth power [19, 80, 81].

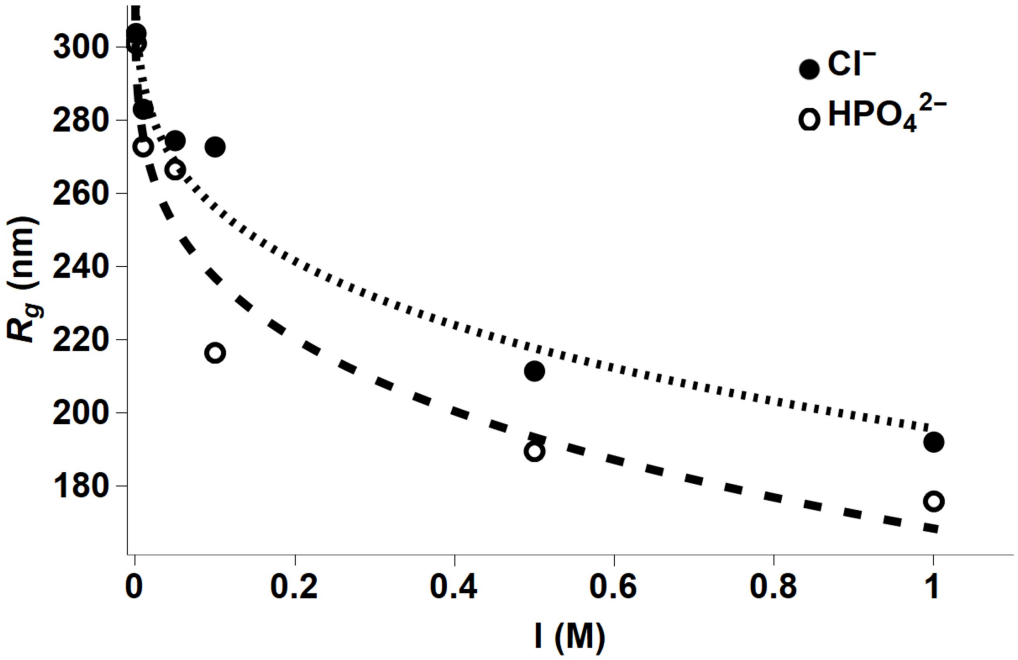

Figure 24: The radius of gyration of pDADMAC (R_g) as a function of the ionic strength of the PE solution for a monovalent (Cl^-) and divalent (HPO_4^{2-}) counterion. The dashed lines are guides for the eyes.

To improve the results of these measurements a finer filter could be used to remove the larger clusters from the sample. Another option would be to perform dynamic light scattering (DLS) as this technique is able to identify all clusters of different sizes in a solution. It is expected, however, that the trend of Figure 24 can nevertheless be transferred to individual polymer chains. Zhang *et al.* showed that the reduction in size of poly(styrene sulfonate) clusters due to the presence of divalent counterions is of the same order as the reduction of R_g of individual chains in the presence of divalent counterions [82].

4.2 Modelling electroosmotic flow

A COMSOL Multiphysics model was correlated with the EOF measurements.

4.2.1 Validation of EOF measurements

EOF simulations were performed using the zeta-potentials as determined from streaming potential measurements of high MW pDADMAC coated capillaries (Section 4.1). Calculating μ_{EO} from the simulations shows that the model consistently produces higher values for μ_{EO} than those found from streaming potential measurements (Figure 25).

This implies that the EOF introduces a systematic overestimate in the

determination of μ_{EO}. The diffusion of rhodamine B, which was used as a marker to determine the EOF, potentially affects the accuracy in calculation of μ_{EO}. To investigate this, the COMSOL model is used to probe the effect of diffusion of rhodamine B on EOF.

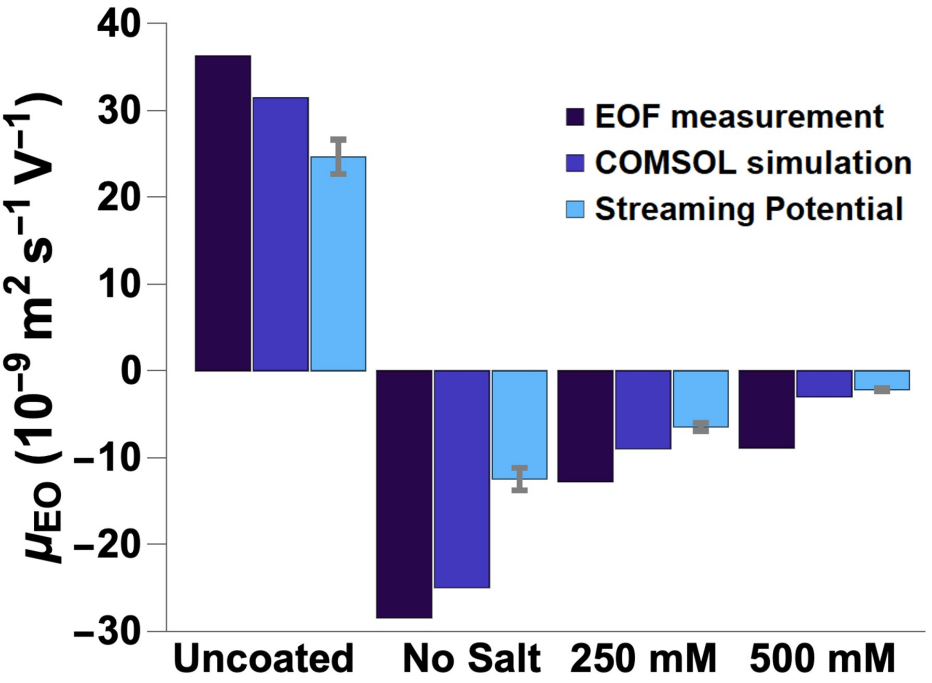

Figure 25: Comparison of values for μ_{EO} found by analyzing the EOF, streaming potential measurements, and the COMSOL model using the experimentally determined zeta-potentials.

4.2.2 Dye front broadening due to diffusion

Experimental determination of the EOF using rhodamine B as a marker showed the front of the dye broadening as it migrated through the capillary. This is reflected in a decrease in the slope of MGV curves measured along the capillary (Figure 26 (a)). This broadening of the dye front could also be observed in EOF simulations with COMSOL (Figure 26 (b)) and is due to the diffusion of rhodamine B in the capillary. The diffusion coefficient (D_c) of *Sp*.1 was varied, while all other input values were constant. This showed that the slope of the MGV curve decreased for higher values of D_c (Figure 27).

This finding underscores that broadening of the dye front is a result of diffusion. The broadening will be more pronounced for MGV curves measured more towards the end of the capillary, as this corresponds to a longer dye travel time. The longer travel time allows for more diffusion to take place.

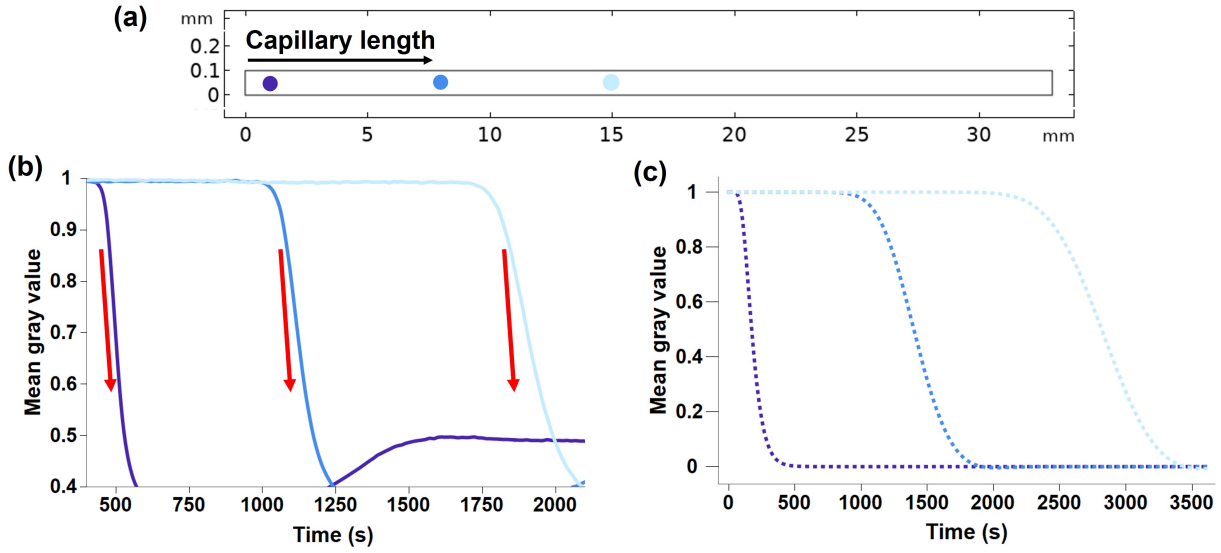

Figure 26: **(a)** The capillary model in COMSOL indicating the positions where the MGV was measured along the length of the capillary with the blue dots. **(b)** Experimental data of MGV curves measured along the length of the capillary. The red arrows indicate the slope of the dark blue curve and are placed next to the blue and light blue curve to visualize the decrease in slope. **(c)** MGV curves from a COMSOL showing the decrease in slope for the curves measured further along the channel. The input of the model corresponds to the experimental conditions in (a).

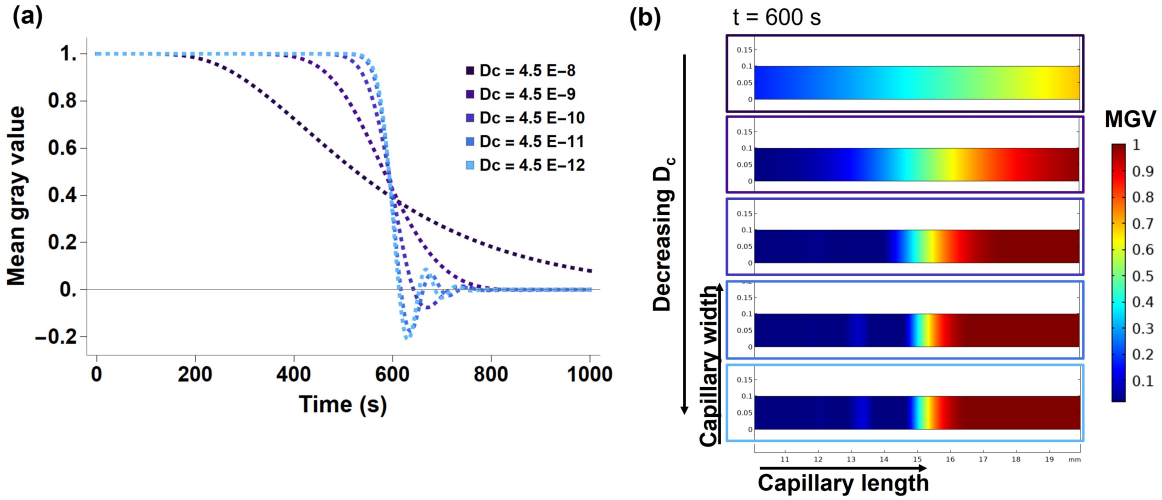

Figure 27: **(a)** MGV curves showing the decrease in slope for higher diffusion coefficients (D_c). The curves were measured at the same position in the channel and all other input variable were kept constant. **(b)** Snapshots from COMSOL simulations showing the broadening of the dye front for increasing D_c at a constant time of 600 s and a fixed location in the capillary. The color map corresponds to the MGV.

4.3 Validation of electrophoretic mobility measurements

Having shown control and suppression of EOF the capillary cell set-up was used to measure electrophoretic mobilities (μ_{EP}). To validate the determined μ_{EP}, measurements of μ_{EP} for Fluorescein (FL) were performed. FL was chosen as its electrophoretic behavior is well reported in literature [83–87]. μ_{EP} measurements of FL were performed at three different ionic strengths (Table 4). The pH was kept constant at pH 7.95 using a phosphate buffer. The capillary was coated with pDADMAC (MW 400–500 kDa, 500 mM NaCl). The capillary was flushed with 2 M NaOH after each measurement, after which the coating was reapplied. The observed μ_{EP} was corrected for EOF by measuring this separately for each experiment giving $\mu_{EP,corrected}$

Table 4: Observed electrophoretic mobility $\mu_{EP,observed}$ of fluorescein for different ionic strength. $\mu_{EP,observed}$ was corrected for electroosmotic flow by adding μ_{EO} to $\mu_{EP,observed}$, giving $\mu_{EP,corrected}$.

I (mM)	$\boldsymbol{\mu_{EP,observed}}^*$	$\boldsymbol{\mu_{EO}}^*$	$\boldsymbol{\mu_{EP,corrected}}^*$
24.4	23.6	-2.7	20.9
48.8	7.4	-	7.4
97.6	6.3	-	6.3

*) $\times 10^{-9}$ $m^2\,V^{-1}\,s^{-1}$

Literature values for μ_{EP} of FL range from 33 to 40 $\times 10^{-9}$ $m^2\,V^{-1}\,s^{-1}$ [83–87]. The values of $\mu_{EP,corrected}$ are out of this range. However, two factors need to be considered carefully:

First, the literature values correspond to a dianionic state of FL. FL has two pKa values corresponding to the deprotonation of an acid group and a hydroxyl group. The charge of FL determines the Coulomb force acting on the molecule and in turn influences the electrophoretic transport behavior. The dissociation of the protons is dependent on the pH. As shown in Figure 28, a neutral state at low pH, a monoanionic state around neutral pH, and a dianionic state at high pH (pH > 8) can be identified [67,83,88,89]. The electrophoretic mobility measurements presented here were controlled at pH 7.95. It can thus be assumed that the reported $\mu_{EP,corrected}$ in Table 4 correspond to the dianionic state of FL.

Second, reported values for μ_{EP} correspond to the *absolute* electrophoretic mobility ($\mu_{EP,abs}$). This value is defined as the mobility of a species at zero ionic strength [83, 90]. As it is experimentally not feasible to achieve such low salt concentrations, we need to extrapolate $\mu_{EP,abs}$ from measurements at higher ionic strengths.

Various theoretical, empirical, and approximate models have been proposed to describe the influence of the ionic strength on μ_{EP} [84,90–92]. Li *et al.* proposed the empirical relation in Equation (19) which corrects the abso-

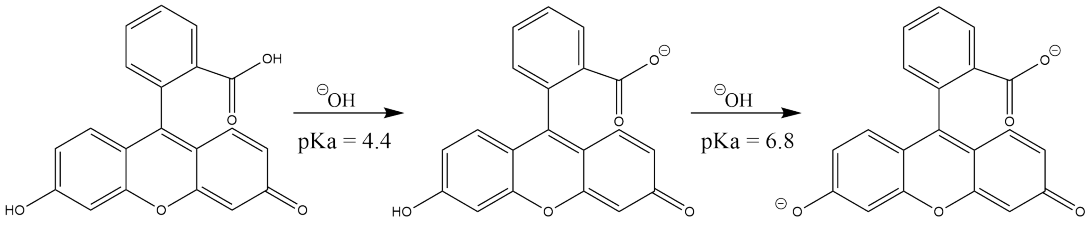

Figure 28: Chemical structure of fluorescein at different pH values. From left to right the pH increases corresponding with a neutral species, monoanionic state, and a dianionic state. The pKa values for the corresponding proton dissociation are given [67, 88, 89].

lute mobility for the ionic strength [92]. This is based on a theoretical model given by Onsager and Fuoss [93] which was corrected by Pitts to account for the finite size of ions [94].

$$\mu_{obs} = \mu_{abs} - A\frac{\sqrt{I}}{1 + B\sqrt{I}} \tag{19}$$

With μ_{obs} the observed value for the electrophoretic mobility at a given ionic strength, and μ_{abs} the absolute value at zero ionic strength. A is a constant depending on the nature of the electrolyte solution and temperature which is taken as a fit parameter [91, 92]. B is a constant that accounts the finite size of the ions and depends on the ionic radii of all ions present [90,92]. B has a value between $1 - 2$ [92]. We have chosen to set it to a value of 1.3 as this gave the best result for our fit.

The absolute mobility $\mu_{EP,abs}$ can now be determined for FL by plotting $\mu_{EP,corrected}$ against $\sqrt{I}/(1 + 1.3\sqrt{I})$ (Figure 29). $|\mu_{EP,abs}|$ then follows from the intercept of the linear fit with the y-axis. We report the absolute value, neglecting the sign of the mobility which indicates towards which electrode FL migrates.

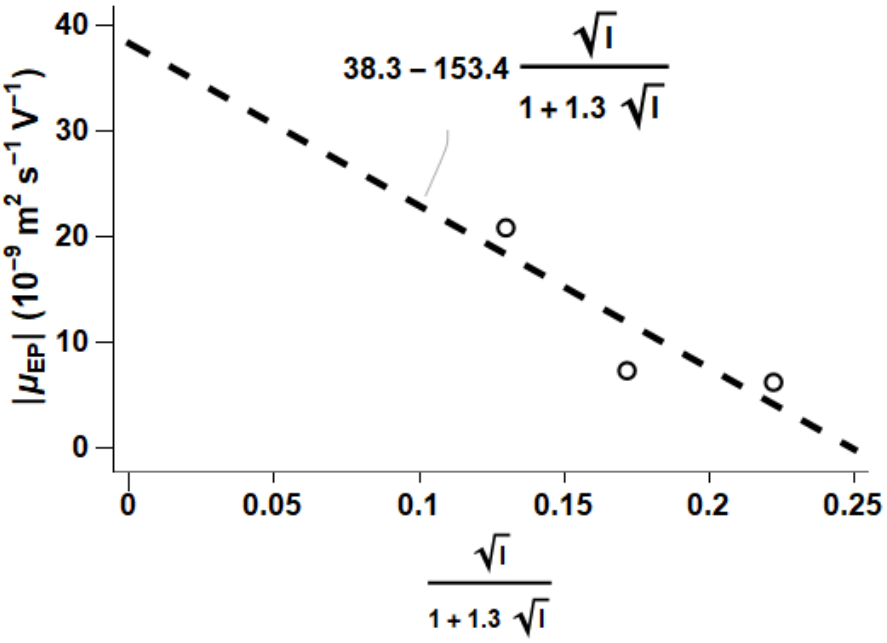

Figure 29: The electrophoretic mobility $|\mu_{EP}|$ of fluorescein in dependence of ionic strength. The circles represent the measured data points. The linear fit is given by equation (19).

Extrapolating the linear fit to zero ionic strength gives $|\mu_{EP,abs}| \approx 38.3 \times 10^{-9}\mathrm{m}^2\,\mathrm{V}^{-1}\,\mathrm{s}^{-1}$ for FL (Figure 29). This is in agreement with literature values [83–87]. The μ_{EP} measurements were only performed once. As a result the correlation coefficient R^2 for the linear fit is only 0.76 and no indication for the spread of $|\mu_{EP,abs}|$ can be provided. It is, however, expected that the linearization of Equation (19) holds and that R^2 will improve with repetitive measurements.

We have shown that reliable electrophoretic mobility measurements can be performed using the capillary cell setup. pH dependent dissociation of the analyte should be taken into account, and correction for the ionic strength using Equation (19) yield the absolute electrophoretic mobility $|\mu_{EP,abs}|$.

4.4 Electrophoretic mobility measurements

μ_{EP} measurements were performed on a model PE using the validated method described in the previous section. Poly(allylamine hydrochloride) (PAH) was chosen as model PE. The structure and protonation behavior of PAH are given in Figure 30 (a) [41]. PAH is colorless when dissolved in water [95]. Fluorescently labeled PAH, poly(fluorescein isothiocyanate allylamine hydrochloride) (PAH-FITC), allows for the determination of μ_{EP} using the capillary cell (Figure 30 (b)). To this end, first the experimental conditions were optimized for the fluorescence and solubility of PAH-FITC.

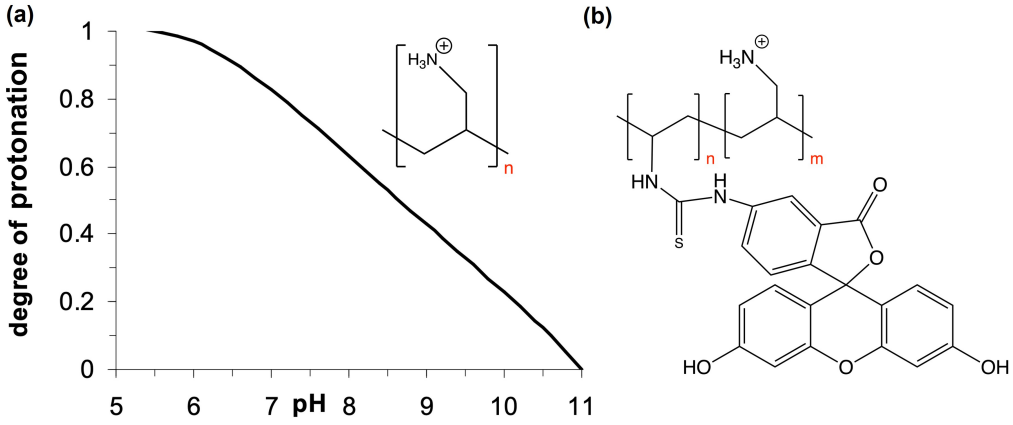

Figure 30: **(a)** Structure of poly(allylamine hydrochloride) and degree of protonation as function of pH, adapted from [41]. **(b)** Structure of poly(fluorescein isothiocyanate allylamine hydrochloride) with $m : n = 50 : 1$.

4.4.1 Experimental considerations

To determine optimized experimental conditions for measuring μ_{EP} of PAH-FITC the fluorescence of PAH-FITC was investigated as a function of the pH (Figure 31 (a)). The fluorescence spectrum of PAH-FITC shows a peak intensity around 518 nm. Plotting the normalized intensity at 518 nm against the pH shows a maximum fluorescence intensity between pH $8-11$ (Figure 31 (a)).

The fluorescence of PAH-FITC and dissolved FL is similar in the range from acidic pH to pH 10 (Figure 31 (a, b)). FL fluorescence intensity plateaus above pH 10 [96,97]. For PAH-FITC the fluorescence intensity drops at more basic pH.

To explain the fluorescence behavior of PAH-FITC, the solubility of PAH-FITC needs to be considered. At low pH the degree of dissociation is of PAH is high. The chain is highly charged and can interact with polar solvents like water (Figure 31 (c)). This corresponds to a high solubility. However, the conjugated FITC group will be neutrally charged (Figure 31 (c)). At pH > 10, PAH is almost completely uncharged and not able to form polar interactions with water while the FITC is charged at this pH (Figure 31 (d)). As the FITC label is only attached to one in every 50 monomers the PAH chain will likely dominate the solubility behavior.

From both the fluorescence signal and solubility of PAH-FITC in water, a pH range of $4-5$ was chosen for the determination of μ_{EP}. In this pH range the PAH chain is fully charged enhancing the solubility. The fluorescence is between $40\% - 50\%$ of the relative maximum intensity.

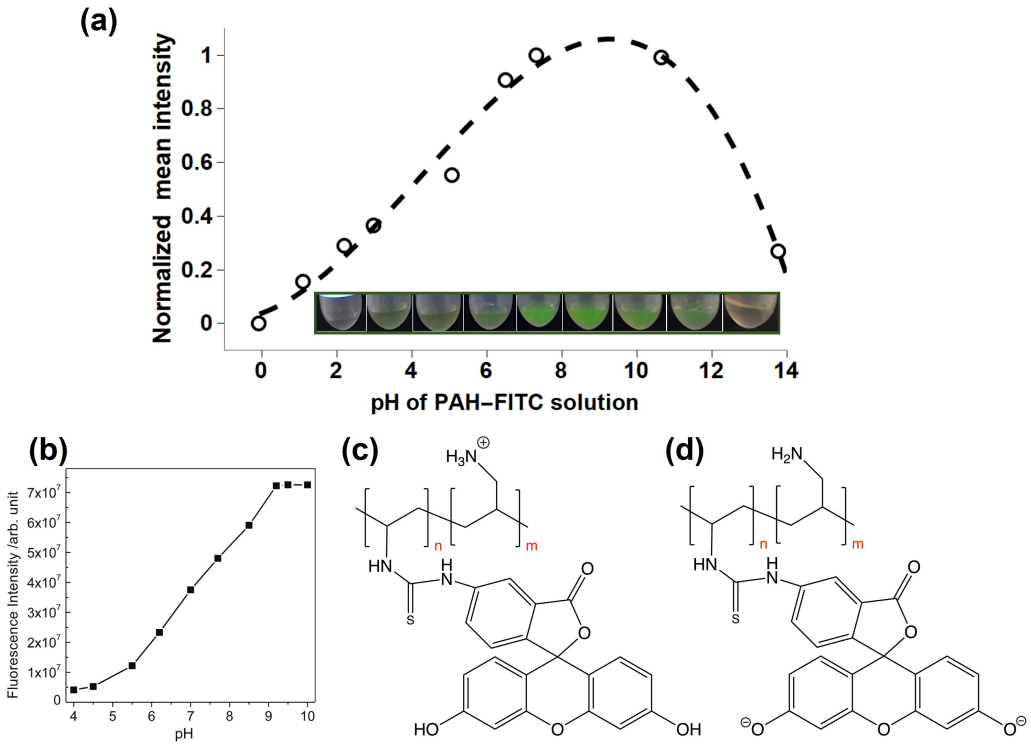

Figure 31: **(a)** Normalized fluorescence intensity of PAH-FITC at different pH values. Excitation wavelength 488 nm. Fluorescence emission detected at 518 nm. The open circles represent the measured data, the dashed line is a guide for the eyes. The inset shows photographs of PAH-FITC solutions at the pH of the data points upon UV-light excitation at 254 nm. **(b)** Fluorescence intensity of FL as function of the pH. Adapted from [96]. **(c)** Protonation PAH-FITC at low pH. **(d)** Dissociation of PAH-FITC at high pH.

4.4.2 Electrophoretic mobility of PAH-FITC

The absolute mobility $\mu_{EP,abs}$ for the fully charged PAH-FITC was determined using the same procedure as described in section 4.3 (Figure 32). The ionic strength was adjusted by diluting the background electrolyte to 20 and 40 mM. Including the contribution of PAH-FITC, the final ionic strengths are given in Table 5. The pH of the background electrolyte was checked before each measurement. The values for μ_{EP} were corrected for EOF by measuring this separately after each run.

$\mu_{EP,corrected}$ was plotted against $\sqrt{I}/(1+1.3\sqrt{I})$ according to Equation (19) (Figure 32). Extrapolating the linear fit ($R^2 = 0.96$) to zero ionic strength gives an absolute electrophoretic mobility of $|\mu_{EP,abs}| = 43.9\times10^{-9}\ \mathrm{m^2\,V^{-1}\,s^{-1}}$. We again report the absolute value of $\mu_{EP,abs}$ which neglects the direction of the migration in the electric field. However, PAH-FITC migrated in opposite direction to FL in the applied electric field, corresponding to the different sign of their charges.

Table 5: Observed electrophoretic mobility $\mu_{EP,observed}$ of PAH-FITC for different ionic strength. $\mu_{EP,observed}$ was corrected for electroosmotic flow by adding μ_{EO} to $\mu_{EP,observed}$, giving $\mu_{EP,corrected}$.

I (mM)	$\mu_{EP,observed}$*	μ_{EO}*	$\mu_{EP,corrected}$*
25.4	20.33	-3.44	23.77
45.4	21.79	-	21.79
109.6	8.91	-1.15	10.06

*) $\times 10^{-9}$ $m^2\,V^{-1}\,s^{-1}$

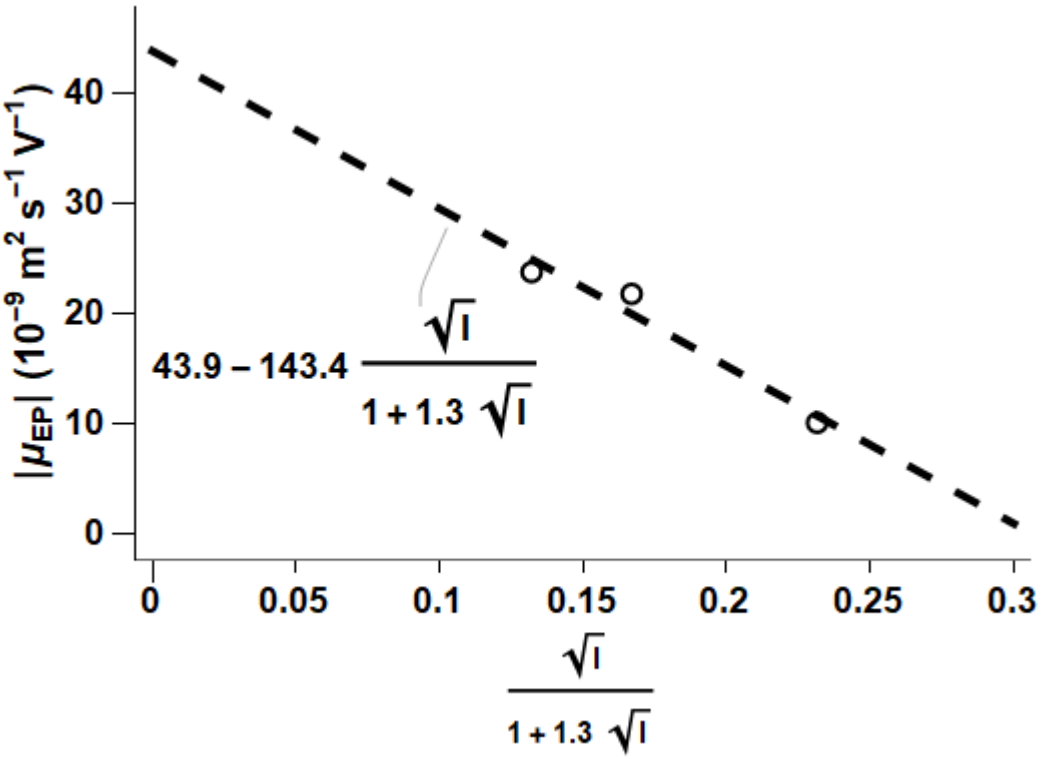

Figure 32: The electrophoretic mobility $|\mu_{EP}|$ of PAH-FITC in dependence of the ionic strength. The circles represent the data points. The linear fit is given by Equation (19).

$\mu_{EP,abs}$ values for PEs are not readily available in literature. However, reported values of $|\mu_{EP,abs}| = 40 - 50 \times 10^{-9}$ $m^2\,V^{-1}\,s^{-1}$ are known for PAH, which is in agreement with the value reported here [45, 98].

Comparing $|\mu_{EP}|$ values reported for other PEs can further validate our findings. $|\mu_{EP}|$ of poly(2-acrylamido-2-methyl-1-propane sulfonic acid) (pAMPS, MW_{avg} $3 \times 10^5 - 10^6$ g/mol) ranges from $50 - 40 \times 10^{-9}$ $m^2\,V^{-1}\,s^{-1}$ for ionic strengths of $0 - 100$ mM [99]. pAMPS is a strong polyelectrolyte, meaning that it has a high charge density like PAH-FITC at the experimental pH of 4.2. Swords *et al.* investigated the EOF through a capillary coated with a PAH/PSS multilayer. Under the assumption that electrophoresis is treated as

the reverse of electroosmosis in their study, the found electroosmotic mobilities may be indicative for $|\mu_{EP}|$ for the top PE layer. Swords *et al.* report values for $|\mu_{EO}|$ ranging from 35 to 45×10^{-9} $m^2\,V^{-1}\,s^{-1}$ for a 3-layer PAH/PSS coating with PAH as top layer in the pH range $7.1 - 5.1$ [100]. Lastly, various authors have found values for $|\mu_{EP}|$ from 10 to 30×10^{-9} $m^2\,V^{-1}\,s^{-1}$ for poly(acrylic acid) depending on the degree of dissociation [101–103].

The determined $|\mu_{EP,abs}|$ for PAH-FITC of 43.9×10^{-9} $m^2\,V^{-1}\,s^{-1}$ corresponds to the above-mentioned literature values of $|\mu_{EP,abs}|$ for PAH, and is in the same order of magnitude as other examples of $|\mu_{EP}|$ for PEs in literature. However, repetitive measurements are needed to further validate the electrophoretic mobility for PAH-FITC.

5 Conclusions

In this thesis electrokinetic transport of polyelectrolytes (PEs) through capillaries was investigated.

Control over the electroosmotic flow (EOF) through capillaries was achieved by applying a pDADMAC coating. Measurements of the electroosmotic mobility (μ_{EO}) showed that μ_{EO} decreases with increasing ionic strength during the coating procedure. This trend was independent of the molecular weight of pDADMAC in the range 100–500 kDa. To regulate the EOF, the phosphate buffer played an important role. From static light scattering experiments it was concluded that the divalent hydrogen phosphate can induce a conformational rearrangement of the pDADMAC chain. This reduces the zeta-potential of the pDADMAC coated capillary, resulting in a reduction of the EOF.

Streaming potential measurements resulted in systematically lower μ_{EO} compared to EOF analysis. A numerical simulation of the EOF was used to explain the deviation of μ_{EO} between the EOF and streaming potential measurements. We found that the diffusion of the analyte introduces a systematic overestimate in the analysis of the EOF through a capillary.

A capillary cell was designed that allowed to accurately determine electrophoretic mobilities (μ_{EP}). Electrophoretic mobility measurements were validated by analyzing μ_{EP} for fluorescein at different ionic strengths. An absolute electrophoretic mobility of $|\mu_{EP,abs}| = 38.3 \times 10^{-9} \mathrm{m^2\,V^{-1}\,s^{-1}}$ was found. This is in agreement with literature, allowing for the determination of $|\mu_{EP,abs}|$ of a PE.

Poly(fluorescein isothiocyanate allylamine hydrochloride) (PAH-FITC) was used as a model PE. The absolute electrophoretic mobility of PAH-FITC was determined to be $|\mu_{EP,abs}| = 43.9 \times 10^{-9}\ \mathrm{m^2\,V^{-1}\,s^{-1}}$. This is in agreement with reported values in literature.

This work has provided a validated experimental setup to study electrokinetic transport of PEs in a controlled manner. It is a stepping stone to future research on electric field assisted PE(-multilayer) assembly onto porous substrates.

6 Outlook

In future work the adsorption of pDADMAC in the presence of divalent counterions should be further investigated by dynamic light scattering (DLS) experiments of pDADMAC dissolved in the presence of monovalent and divalent counterions. This could further validate the proposed mechanism conformational rearrangement of adsorbed pDADMAC in the presence of divalent counterions. Measurements of electrophoretic mobilities of polyelectrolytes (PEs) can be performed to characterize the electrophoretic migration of PEs for varying pH and charge density of the PE.

The effect of deposition of alternately charged PEs on the electrokinetic transport behavior of PEs should be investigated. This knowledge could be used to govern the assembly of homogeneous and selective PE separation layers on and in porous substrates.

Acknowledgements

This work would not have been possible without the continued help and support of a number of important people. I would first like to thank Martin Haase for allowing me to join his research group to do this project. I value the discussions we have had about my results, the guidance you have given me in performing research, and of course the nice conversations we have had that had nothing to do with research. Next, I owe a lot of thanks to Henrik, whose door was always open for my questions and who took an active role in supervising my research. Thank you for your help in the lab, making sense of the research results, helping me write it all up, and all your advice. You have been kind and understanding, while still pushing me to be the most productive version of myself.

I want to thank Bonny Kuipers for his excellent help with the SLS experiments. Thanks to everyone from the Haase research group for always being available for questions and the nice discussions during the group meetings. The technicians at the Physical and Colloid Chemistry group are thanked for keeping the lab safe and running. Everyone at the Physical and Colloid Chemistry group is thanked for creating such a nice working environment.

A special thanks is owed to Jip. Thank you for your support, love, kindness, and patience. Thank you for listening to my incoherent ramblings and frustrations, and celebrating my victories. You keep me going.

I want to thank all my dear friends from "donderdagavond" and all the master students at FCC for making sure life wasn't all about my master thesis. Thanks for all the drinks, parties, laughs, and memes.

Finally, I would like to thank my parents, without whom I would have never gotten where I am today.

References

[1] M. M. Mekonnen and A. Y. Hoekstra, "Four billion people facing severe water scarcity," *Science Advances*, vol. 2, no. 2, p. e1500323, 2016. [Online]. Available: https://www.science.org/doi/abs/10.1126/sciadv.1500323

[2] M. Kumar and H. A. Stone, "Membrane science emerging as a convergent scientific field with molecular origins and understanding, and global impact," *Proceedings of the National Academy of Sciences*, vol. 118, no. 37, p. e2106494118, 2021. [Online]. Available: https://www.pnas.org/doi/abs/10.1073/pnas.2106494118

[3] M. A. Shannon, P. W. Bohn, M. Elimelech, J. G. Georgiadis, B. J. Mariñas, and A. M. Mayes, "Science and technology for water purification in the coming decades," *Nature*, vol. 452, no. 7185, pp. 301–310, 2008. [Online]. Available: https://doi.org/10.1038/nature06599

[4] P. Zhang, J. Qian, Y. Yang, Q. An, X. Liu, and Z. Gui, "Polyelectrolyte layer-by-layer self-assembly enhanced by electric field and their multilayer membranes for separating isopropanol-water mixtures," *Journal of Membrane Science*, vol. 320, pp. 73–77, 7 2008.

[5] Q. Zhao, Q. F. An, Y. Ji, J. Qian, and C. Gao, "Polyelectrolyte complex membranes for pervaporation, nanofiltration and fuel cell applications," *Journal of Membrane Science*, vol. 379, no. 1, pp. 19–45, 2011. [Online]. Available: https://www.sciencedirect.com/science/article/pii/S0376738811004558

[6] N. Joseph, P. Ahmadiannamini, R. Hoogenboom, and I. F. Vankelecom, "Layer-by-layer preparation of polyelectrolyte multilayer membranes for separation," *Polymer Chemistry*, vol. 5, pp. 1817–1831, 3 2014.

[7] J. de Grooth, R. Oborný, J. Potreck, K. Nijmeijer, and W. M. de Vos, "The role of ionic strength and odd-even effects on the properties of polyelectrolyte multilayer nanofiltration membranes," *Journal of Membrane Science*, vol. 475, pp. 311–319, 2 2015.

[8] X. Liu and M. L. Bruening, "Size-selective transport of uncharged solutes through multilayer polyelectrolyte membranes," *Chemistry of Materials*, vol. 16, no. 2, pp. 351–357, 2004. [Online]. Available: https://doi.org/10.1021/cm034559k

[9] M. Hess, R. G. Jones, J. Kahovec, T. Kitayama, P. Kratochvíl, P. Kubisa, W. Mormann, R. F. T. Stepto, D. Tabak, J. Vohlídal, and E. S. Wilks, "Terminology of polymers containing ionizable or ionic groups and of polymers containing ions (iupac recommendations

2006)," *Pure and Applied Chemistry*, vol. 78, no. 11, pp. 2067–2074, 2006. [Online]. Available: https://doi.org/10.1351/pac200678112067

[10] J. Choi and M. F. Rubner, "Influence of the degree of ionization on weak polyelectrolyte multilayer assembly," *Macromolecules*, vol. 38, pp. 116–124, 1 2005.

[11] S. Owusu-Nkwantabisah and C. P. Tripp, "Controlled growth of layer-by-layer assembled polyelectrolyte multilayer films under high electric fields," *Journal of Colloid and Interface Science*, vol. 541, pp. 322–328, 4 2019.

[12] Y. H. Ko, Y. H. Kim, J. Park, K. T. Nam, J. H. Park, and P. J. Yoo, "Electric-field-assisted layer-by-layer assembly of weakly charged polyelectrolyte multilayers," *Macromolecules*, vol. 44, pp. 2866–2872, 4 2011.

[13] A. P. Ngankam and P. R. V. Tassel, "Sciences of the usa 1140-1145 pnas," 2007.

[14] Y. Omura, K. H. Kyung, S. H. Kim, and S. Shiratori, "Investigation of the effects caused by applying voltage in layer-by-layer self-assembly method," *MATEC Web of Conferences*, vol. 4, 2013. [Online]. Available: http://dx.doi.org/10.1051/matecconf/20130405009

[15] C. Olsen and P. R. V. Tassel, "Polyelectrolyte adsorption kinetics under an applied electric potential: Strongly versus weakly charged polymers," *Journal of Colloid and Interface Science*, vol. 329, pp. 222–227, 1 2009.

[16] G. Zhang, X. Gao, S. Ji, and Z. Liu, "Electric field-enhanced assembly of polyelectrolyte composite membranes," *Journal of Membrane Science*, vol. 307, pp. 151–155, 1 2008.

[17] T. Wang, J. Lu, L. Mao, and Z. Wang, "Electric field assisted layer-by-layer assembly of graphene oxide containing nanofiltration membrane," *Journal of Membrane Science*, vol. 515, pp. 125–133, 10 2016.

[18] M. A. Khan, A. J. Sprockel, K. A. Macmillan, M. T. Alting, S. P. Kharal, S. Boakye-Ansah, M. F. Haase, M. A. Khan, A. J. Sprockel, K. A. Macmillan, M. T. Alting, M. F. Haase, S. P. Kharal, and S. Boakye-Ansah, "Nanostructured, fluid-bicontinuous gels for continuous-flow liquid–liquid extraction," *Advanced Materials*, p. 2109547, 3 2022. [Online]. Available: https://onlinelibrary.wiley.com/doi/full/10.1002/adma.202109547https://onlinelibrary.wiley.com/doi/abs/10.1002/adma.202109547https://onlinelibrary.wiley.com/doi/10.1002/adma.202109547

[19] H. R. Kruyt, G. H. Jonker, and J. T. G. Overbeek, *Colloid Science I, Irreversible Systems*, H. R. Kruyt, Ed. Elsevier, 1952.

[20] L. Herbowski, H. Gurgul, and W. Staron, "Experimental determination of the stern layer thickness at the interface of the human arachnoid membrane and the cerebrospinal fluid," *Zeitschrift für Medizinische Physik*, vol. 19, no. 3, pp. 189–192, 2009. [Online]. Available: https://www.sciencedirect.com/science/article/pii/S0939388909000798

[21] H. Zhang, A. A. Hassanali, Y. K. Shin, C. Knight, and S. J. Singer, "The water–amorphous silica interface: Analysis of the stern layer and surface conduction," *The Journal of Chemical Physics*, vol. 134, no. 2, p. 024705, 2011. [Online]. Available: https://doi.org/10.1063/1.3510536

[22] J. Lyklema, "On the slip process in electrokinetics," *Colloids and Surfaces A: Physicochemical and Engineering Aspects*, vol. 92, pp. 41–49, 1994.

[23] N. Soyer, S. Salgın, and U. Salgın, "Streaming potential measurements of polyethersulfone ultrafiltration membranes to determine salt effects on membrane zeta potential," *International Journal of Electrochemical Science*, vol. 8, pp. 4073–4084, 2013.

[24] H.-J. Butt, K. Graf, and M. Kappl, *The Electric Double Layer*. John Wiley and Sons, Ltd, 2003, ch. 4, pp. 42–56. [Online]. Available: https://onlinelibrary.wiley.com/doi/abs/10.1002/3527602313.ch4

[25] D. L. Oatley-Radcliffe, N. Aljohani, P. M. Williams, and N. Hilal, *Electrokinetic Phenomena for Membrane Charge*. Elsevier Inc., 2 2017.

[26] D. Möckel, E. Staude, M. Dal-Cin, K. Darcovich, and M. Guiver, "Tangential flow streaming potential measurements: Hydrodynamic cell characterization and zeta potentials of carboxylated polysulfone membranes," *Journal of Membrane Science*, vol. 145, pp. 211–222, 7 1998.

[27] R. J. Hunter, *Zeta Potential in Colloid Science, Principles and Applications*, R. H. Ottewill and R. L. Rowell, Eds. Academic Press, 1981.

[28] K. J. Kim, A. G. Fane, M. Nystrom, A. Pihlajamaki, W. R. Bowen, and H. Mukhtar, "Evaluation of electroosmosis and streaming potential for measurement of electric charges of polymeric membranes," *Journal of Membrane Science*, vol. 116, pp. 149–159, 1996.

[29] D. L. Oatley-Radcliffe, N. Aljohani, P. M. Williams, and N. Hilal, *Electrokinetic Phenomena for Membrane Charge*. Elsevier Inc., 2 2017.

[30] L. D. Thanh, "Streaming potential in unconsolidated samples saturated with monovalent electrolytes," *VNU Journal of Science: Mathematics - Physics*, vol. 34, 3 2018.

[31] J. Pfitzner, "Poiseuille and his law," *Anaesthesia*, vol. 31, no. 2, pp. 273–275, 1976. [Online]. Available: https://associationofanaesthetists-publications.onlinelibrary.wiley.com/doi/abs/10.1111/j.1365-2044.1976.tb11804.x

[32] K. Avila, D. Moxey, A. de Lozar, M. Avila, D. Barkley, and B. Hof, "The onset of turbulence in pipe flow," *Science*, vol. 333, no. 6039, pp. 192–196, 2011. [Online]. Available: https://www.science.org/doi/abs/10.1126/science.1203223

[33] N. Rott, "Note on the history of the reynolds number," *Annual review of fluid mechanics*, vol. 22, no. 1, pp. 1–12, 1990.

[34] A. Sommerfeld, "Ein beitrag zur hydrodynamischen erklaerung der turbulenten fluessigkeitsbewegungen," *Philos. Trans. R. Soc. B*, vol. 174, 1883. [Online]. Available: https://web.archive.org/web/20161115133937/http://www.mathunion.org/ICM/ICM1908.3/Main/icm1908.3.0116.0124.ocr.pdf

[35] J. T. G. Overbeek and P. H. Wiersema, *Electrophoresis: Theory, Methods, and Applications*, M. Bier, Ed. Academic Press, 1967, vol. 2.

[36] J. L. Viovy, "Electrophoresis of dna and other polyelectrolytes: Physical mechanisms," *Reviews of Modern Physics*, vol. 72, pp. 813–872, 2000.

[37] P. Atkins and J. de Paula, *Atkins' physical chemistry*, 9th ed. Oxford University Press, 2010.

[38] M. C. Stuart, R. de Vries, and H. Lyklema, "Chapter 2 - polyelectrolytes," in *Soft Colloids*, ser. Fundamentals of Interface and Colloid Science, J. Lyklema, Ed., 2005, vol. 5, pp. 2.1–2.84. [Online]. Available: https://www.sciencedirect.com/science/article/pii/S1874567905800066

[39] C. Padeste and S. Neuhaus, "Chapter 1 - functional polymer structures," in *Polymer Micro- and Nanografting*, ser. Micro and Nano Technologies, C. Padeste and S. Neuhaus, Eds. Oxford: William Andrew Publishing, 2015, pp. 1–10. [Online]. Available: https://www.sciencedirect.com/science/article/pii/B9780323353229000012

[40] I. Szilagyi, G. Trefalt, A. Tiraferri, P. Maroni, and M. Borkovec, "Polyelectrolyte adsorption, interparticle forces, and colloidal aggregation," *Soft Matter*, vol. 10, pp. 2479–2502, 4 2014.

[41] M. Haase, "Modification of nanoparticle surfaces for emulsion stabilization and encapsulation of active molecules for anit-corrosive coatings," Ph.D. dissertation, Max Planck Institute of Colloids and Interfaces, University of Potsdam, 2011.

[42] W. M. de Vos and S. Lindhoud, "Overcharging and charge inversion: Finding the correct explanation(s)," *Advances in Colloid and Interface Science*, vol. 274, 12 2019.

[43] J. Lyklema and L. Deschênes, "The first step in layer-by-layer deposition: Electrostatics and/or non-electrostatics?" *Advances in Colloid and Interface Science*, vol. 168, pp. 135–148, 10 2011.

[44] D. K. Kim, S. W. Han, C. H. Kim, J. D. Hong, and K. Kim, "Morphology of multilayers assembled by electrostatic attraction of oppositely charged model polyelectrolytes," *Thin Solid Films*, vol. 350, no. 1, pp. 153–160, 1999. [Online]. Available: https://www.sciencedirect.com/science/article/pii/S004060909900351X

[45] B. Jachimska, T. Jasiński, P. Warszyński, and Z. Adamczyk, "Conformations of poly(allylamine hydrochloride) in electrolyte solutions: Experimental measurements and theoretical modeling," *Colloids and Surfaces A: Physicochemical and Engineering Aspects*, vol. 355, pp. 7–15, 2 2010.

[46] N. G. Hoogeveen, M. A. C. Stuart, and G. J. Fleer, "Polyelectrolyte adsorption on oxides i. kinetics and adsorbed amounts," *Journal of Colloid and Interface Science*, vol. 182, pp. 133–145, 1996.

[47] K. E. Bremmell, G. J. Jameson, and S. Biggs, "Polyelectrolyte adsorption at the solid/liquid interface interaction forces and stability," *Colloids and Surfaces A: Physicochemical and Engineering Aspects*, vol. 139, pp. 199–211, 1998.

[48] D. Volodkin and R. V. Klitzing, "Competing mechanisms in polyelectrolyte multilayer formation and swelling: Polycation-polyanion pairing vs. polyelectrolyte-ion pairing," *Current Opinion in Colloid and Interface Science*, vol. 19, pp. 25–31, 2014.

[49] I. Borukhov, D. Andelman, and H. Orland, "Scaling laws of polyelectrolyte adsorption," *Macromolecules*, vol. 31, no. 5, pp. 1665–1671, 1998. [Online]. Available: https://doi.org/10.1021/ma9707300

[50] J. Meadows, P. Williams, M. Garvey, R. Harrop, and G. Phillips, "Characterization of the adsorption—desorption behavior of hydrolyzed polyacrylamide," *Journal of Colloid and Interface Science*, vol. 132, no. 2, pp. 319–328, 1989. [Online]. Available: https://www.sciencedirect.com/science/article/pii/0021979789902476

[51] M. Kawaguchi, H. Kawaguchi, and A. Takahashi, "Competitive and displacement adsorption of polyelectrolyte and water-soluble nonionic polymer at the silica surface," *Journal of Colloid and Interface Science*, vol. 124, pp. 56–62, 7 1988.

[52] Z. Adamczyk, M. Zembala, P. Warszyński, and B. Jachimska, "Characterization of polyelectrolyte multilayers by the streaming potential method," *Langmuir*, vol. 20, pp. 10 517–10 525, 11 2004.

[53] Z. Adamczyk, M. Zembala, M. Kolasińska, and P. Warszyński, "Characterization of polyelectrolyte multilayers on mica and oxidized titanium by streaming potential and wetting angle measurements," *Colloids and Surfaces A: Physicochemical and Engineering Aspects*, vol. 302, pp. 455–460, 7 2007.

[54] C. Ringwald and V. Ball, "Shear induced changes in the streaming potential of polyelectrolyte multilayer films," *Colloids and Surfaces A: Physicochemical and Engineering Aspects*, vol. 464, pp. 41–45, 1 2015.

[55] A. Shafir and D. Andelman, "Polyelectrolyte adsorption: Chemical and electrostatic interactions," *Physical Review E - Statistical Physics, Plasmas, Fluids, and Related Interdisciplinary Topics*, vol. 70, p. 12, 2004.

[56] J. F. Joanny, "Polyelectrolyte adsorption and charge inversion," *Eur. Phys. J. B*, vol. 9, pp. 117–122, 1999.

[57] H. Siegel, A. J. Sprockel, M. S. Schwenger, J. M. Steenhoff, I. Achterhuis, W. M. de Vos, and M. F. Haase, "Synthesis and polyelectrolyte functionalization of hollow fiber membranes formed by solvent transfer induced phase separation," *ACS Applied Materials & Interfaces*, vol. 14, no. 38, pp. 43 195–43 206, 2022, pMID: 36106768. [Online]. Available: https://doi.org/10.1021/acsami.2c10343

[58] W. Jin, A. Toutianoush, and B. Tieke, "Use of polyelectrolyte layer-by-layer assemblies as nanofiltration and reverse osmosis membranes," *Langmuir*, vol. 19, no. 7, pp. 2550–2553, 2003. [Online]. Available: https://doi.org/10.1021/la020926f

[59] J. Kamp, S. Emonds, and M. Wessling, "Designing tubular composite membranes of polyelectrolyte multilayer on ceramic supports with nanofiltration and reverse osmosis transport properties," *Journal of Membrane Science*, vol. 620, p. 118851, 2021. [Online]. Available: https://www.sciencedirect.com/science/article/pii/S0376738820314265

[60] D. M. Reurink, J. D. Willott, H. D. Roesink, and W. M. D. Vos, "Role of polycation and cross-linking in polyelectrolyte multilayer

membranes," *ACS Applied Polymer Materials*, vol. 2, pp. 5278–5289, 11 2020.

[61] A. Rudin, *The Elements of Polymer Science and Engineering: An Introductory Text and Reference for Engineers and Chemists*. Academic Press, 1999. [Online]. Available: https://books.google.nl/books?id=zfcBlQEACAAJ

[62] C. D. Putnam, "Guinier peak analysis for visual and automated inspection of small-angle X-ray scattering data," *Journal of Applied Crystallography*, vol. 49, no. 5, pp. 1412–1419, Oct 2016. [Online]. Available: https://doi.org/10.1107/S1600576716010906

[63] R. M. Murphy, "Static and dynamic light scattering of biological macromolecules: what can we learn?" *Current Opinion in Biotechnology*, vol. 8, no. 1, pp. 25–30, 1997. [Online]. Available: https://www.sciencedirect.com/science/article/pii/S095816699780153X

[64] D. R. Latulippe and A. L. Zydney, "Radius of gyration of plasmid dna isoforms from static light scattering," *Biotechnology and Bioengineering*, vol. 107, no. 1, pp. 134–142, 2010. [Online]. Available: https://onlinelibrary.wiley.com/doi/abs/10.1002/bit.22787

[65] A. Guinier and G. Fournet, *Small-angle scattering of X-rays, Translation by C. B. Walker*. John Wiley & Sons, 1955.

[66] A. K. Boal, F. Ilhan, J. E. Derouchey, T. Thurn-Albrecht, T. P. Russell, and V. M. Rotello, "Self-assembly of nanoparticles into structured spherical and network aggregates," pp. 746–748, 2000.

[67] N. O. Mchedlov-Petrossyan, V. I. Kukhtik, and V. I. Alekseeva, "Ionization and tautomerism of fluorescein, rhodamine b, n,n-diethylrhodol and related dyes in mixed and nonaqueous solvents," *Dyes and Pigments*, vol. 24, pp. 11–35, 1994.

[68] P. O. Gendron, F. Avaltroni, and K. J. Wilkinson, "Diffusion coefficients of several rhodamine derivatives as determined by pulsed field gradient-nuclear magnetic resonance and fluorescence correlation spectroscopy," *Journal of Fluorescence*, vol. 18, pp. 1093–1101, 11 2008.

[69] Y. Wang and P. L. Dubin, "Capillary modification by noncovalent polycation adsorption: Effects of polymer molecular weight and adsorption ionic strength," *Analytical Chemistry*, vol. 71, no. 16, pp. 3463–3468, 1999. [Online]. Available: https://doi.org/10.1021/ac990146k

[70] Wolfram Language and System Documentation Center, *How to Fit Models with Measurement Errors*. [Online]. Available: https://reference.wolfram.com/language/howto/FitModelsWithMeasurementErrors.html

[71] W. H. Press, S. A. Teukolsky, W. T. Vetterling, and B. P. Flannery, *Numerical Recipes 3rd Edition: The Art of Scientific Computing*, 3rd ed. Cambridge University Press, 2007. [Online]. Available: http://numerical.recipes/book/book.html

[72] D. Corradini and L. Sprecacenere, "Dependence of the electroosmotic flow in bare fused-silica capillaries from ph, ionic strength and composition of electrolyte solutions tailored for protein capillary zone electrophoresis," *Chromatographia*, vol. 58, no. 9-10, pp. 587–596, 2003.

[73] R. Rehmet and E. Killmann, "Adsorption of cationic poly(diallyl-dimethyl-ammoniumchloride), poly(diallyl-dimethyl-ammoniumchloride-co-n-methyl-n-vinylactamide) and poly(n-methyl-n-vinyl-acetamide) on polystyrene latex," *Colloids and Surfaces A: Physicochemical and Engineering Aspects*, vol. 149, no. 1, pp. 323–328, 1999. [Online]. Available: https://www.sciencedirect.com/science/article/pii/S092777579800329X

[74] K. J. Powell, P. L. Brown, R. H. Byrne, T. Gajda, G. Hefter, S. Sjöberg, and H. Wanner, "Chemical speciation of environmentally significant heavy metals with inorganic ligands. part 1: The hg2+– cl–, oh–, co32–, so42–, and po43– aqueous systems (iupac technical report)," *Pure and Applied Chemistry*, vol. 77, no. 4, pp. 739–800, 2005. [Online]. Available: https://doi.org/10.1351/pac200577040739

[75] D. D. Perrin, "Ionization constants of inorganic acids and bases in aqueous solution, second edition." *Journal of Chemical Education*, vol. 60, p. A151, 5 1983.

[76] P. Atkins and J. de Paula, *Atkins' physical chemistry*, 7th ed. Oxford University Press, 2002.

[77] J. Wei, D. A. Hoagland, G. Zhang, and Z. Su, "Effect of divalent counterions on polyelectrolyte multilayer properties," *Macromolecules*, vol. 49, pp. 1790–1797, 3 2016.

[78] A. Chremos and J. F. Douglas, "Influence of higher valent ions on flexible polyelectrolyte stiffness and counter-ion distribution," *Journal of Chemical Physics*, vol. 144, 4 2016.

[79] H. Dautzenberg, E. Görnitz, and W. Jaeger, "Synthesis and characterization of poly(diallyldimethylammonium chloride) in a broad range of

molecular weight," *Macromolecular Chemistry and Physics*, vol. 199, pp. 1561–1571, 1998.

[80] H. Moosmüller and W. P. Arnott, "Particle optics in the rayleigh regime," *Journal of the Air & Waste Management Association*, vol. 59, no. 9, pp. 1028–1031, 2009. [Online]. Available: https://doi.org/10.3155/1047-3289.59.9.1028

[81] J. H. Seinfeld and S. N. Pandis, *Atmospheric chemistry and physics : from air pollution to climate change.* J. Wiley, 2006.

[82] Y. Zhang, J. F. Douglas, B. D. Ermi, and E. J. Amis, "Influence of counterion valency on the scattering properties of highly charged polyelectrolyte solutions," *Journal of Chemical Physics*, vol. 114, pp. 3299–3313, 2 2001.

[83] D. Milanova, R. D. Chambers, S. S. Bahga, and J. G. Santiago, "Electrophoretic mobility measurements of fluorescent dyes using on-chip capillary electrophoresis," *Electrophoresis*, vol. 32, no. 22, pp. 3286–3294, 2011. [Online]. Available: https://analyticalsciencejournals.onlinelibrary.wiley.com/doi/abs/10.1002/elps.201100210

[84] A. Persat, M. E. Suss, and J. G. Santiago, "Basic principles of electrolyte chemistry for microfluidic electrokinetics. part ii: Coupling between ion mobility, electrolysis, and acid–base equilibria," *Lab on a Chip*, vol. 9, pp. 2454–2469, 9 2009. [Online]. Available: https://pubs.rsc.org/en/content/articlehtml/2009/lc/b906468khttps://pubs.rsc.org/en/content/articlelanding/2009/lc/b906468k

[85] Y. Shakalisava, M. Poitevin, J.-L. Viovy, and S. Descroix, "Versatile method for electroosmotic flow measurements in microchip electrophoresis," *Journal of Chromatography A*, vol. 1216, no. 6, pp. 1030–1033, 2009. [Online]. Available: https://www.sciencedirect.com/science/article/pii/S0021967308021985

[86] P. H. Paul, M. G. Garguilo, and D. J. Rakestraw, "Imaging of pressure- and electrokinetically driven flows through open capillaries," *Analytical Chemistry*, vol. 70, no. 13, pp. 2459–2467, 1998, pMID: 21644766. [Online]. Available: https://doi.org/10.1021/ac9709662

[87] C. W. Whang and E. S. Yeung, "Temperature programming in capillary zone electrophoresis," *Analytical Chemistry*, vol. 64, no. 5, pp. 502–506, 1992. [Online]. Available: https://doi.org/10.1021/ac00029a010

[88] L. D. Lavis, T. J. Rutkoski, and R. T. Raines, "Tuning the pka of fluorescein to optimize binding assays," *Analytical Chemistry*, vol. 79, no. 17, pp. 6775–6782, 2007, pMID: 17672523. [Online]. Available: https://doi.org/10.1021/ac070907g

[89] N. Klonis and W. H. Sawyer, "Spectral properties of the prototropic forms of fluorescein in aqueous solution," *Journal of Fluorescence*, vol. 6, 1996.

[90] S. S. Bahga, M. Bercovici, and J. G. Santiago, "Ionic strength effects on electrophoretic focusing and separations," *Electrophoresis*, vol. 31, pp. 910–919, 3 2010.

[91] S. P. Porras, M. L. Riekkola, and E. Kenndler, "The principles of migration and dispersion in capillary zone electrophoresis in nonaqueous solvents," pp. 1485–1498, 5 2003.

[92] D. Li, S. Fu, and C. A. Lucy, "Prediction of electrophoretic mobilities. 3. effect of ionic strength in capillary zone electrophoresis," *Analytical Chemistry*, vol. 71, pp. 687–699, 2 1999.

[93] L. Onsager and R. M. Fuoss, "Irreversible processes in electrolytes. diffusion, conductance and viscous flow in arbitrary mixtures of strong electrolytes," *The Journal of Physical Chemistry*, vol. 36, no. 11, pp. 2689–2778, 1932. [Online]. Available: https://doi.org/10.1021/j150341a001

[94] E. Pitts and B. E. Tabor, "Concentration dependence of electrolyte conductance. part 2.—comparison of experimental data with the fuoss-onsager and pitts treatments," *Trans. Faraday Soc.*, vol. 66, pp. 693–707, 1970. [Online]. Available: http://dx.doi.org/10.1039/TF9706600693

[95] Merck Life Science N.V., "poly(allylamine) solution," Amsterdam, The Netherlands, 2020. [Online]. Available: https://www.sigmaaldrich.com/NL/en/sds/aldrich/479136

[96] M. Liu, M. Jia, H. Pan, L. Li, M. Chang, H. Ren, F. Argoul, S. Zhang, and J. Xu, "Instrument response standard in time-resolved fluorescence spectroscopy at visible wavelength: quenched fluorescein sodium," *Applied spectroscopy*, vol. 68, pp. 577–583, 2014.

[97] E. A. Slyusareva, M. A. Gerasimov, A. G. Sizykh, and L. M. Gornostaev, "Spectral and fluorescent indication of the acid-base properties of biopolymer solutions," *Russian Physics Journal*, vol. 54, 2011.

[98] M. Morga and Z. Adamczyk, "Monolayers of cationic polyelectrolytes on mica - electrokinetic studies," *Journal of Colloid and Interface Science*, vol. 407, pp. 196–204, 10 2013.

[99] I. Desvignes, J. Chamieh, and H. Cottet, "Separation and characterization of highly charged polyelectrolytes using free-solution

capillary electrophoresis," *Polymers*, vol. 10, no. 12, 2018. [Online]. Available: https://www.mdpi.com/2073-4360/10/12/1331

[100] K. E. Swords, P. B. Bartline, K. M. Roguski, S. A. Bashaw, and K. A. Frederick, "Assessment of polyelectrolyte coating stability under dynamic buffer conditions in ce," *Journal of Separation Science*, vol. 34, no. 18, pp. 2427–2432, 2011. [Online]. Available: https://analyticalsciencejournals.onlinelibrary.wiley.com/doi/abs/10.1002/jssc.201100044

[101] D. A. Hoagland, D. L. Smisek, and D. Y. Chen, "Gel and free solution electrophoresis of variability charged polymers," *Electrophoresis*, vol. 17, pp. 1151–1160, 6 1996.

[102] E. Prokopova and V. Vitagliarqo, "Electrophoretic heterogeneity of polymethacrylic, polyacrylic and polyethylenesulphonic acid in nac1," *European Polymer Journal*, vol. 8, pp. 851–859, 1972.

[103] I. Noda, M. Nagasawa, and M. Ota, "Electrophoresis of a polyelectrolyte in solutions of high ionic strength," *J. Chem. Phys*, vol. 86, p. 900, 1964.

Appendix A

Photos of experimental setups

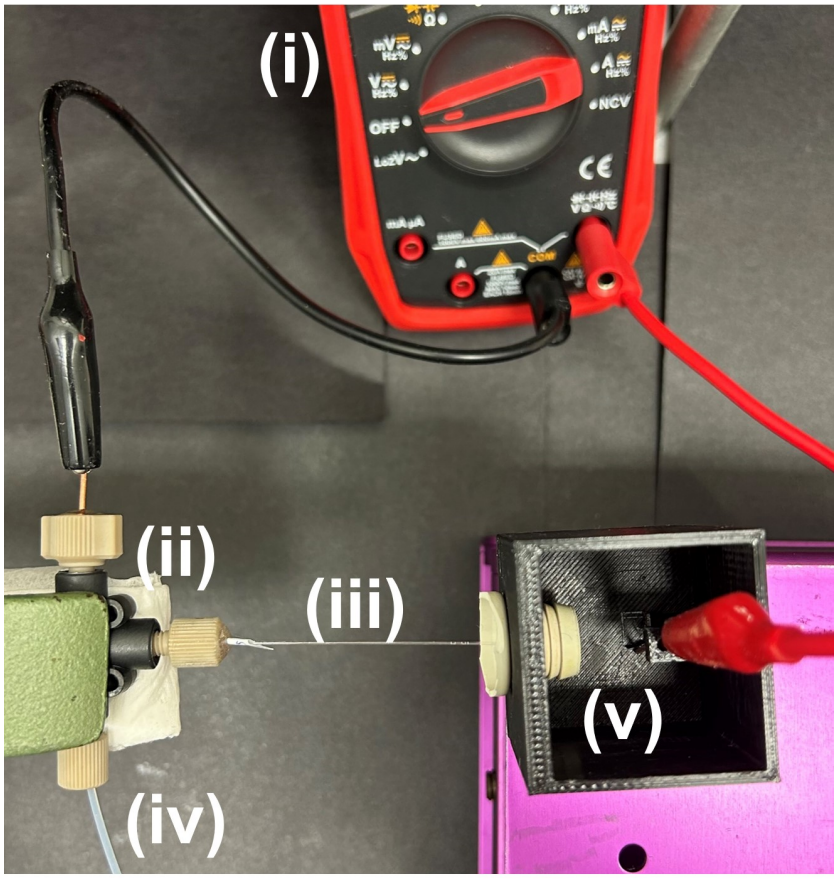

Figure 33: Photograph of the setup used to measure the streaming potential of the inner wall of a round capillary. (*i*) Voltmeter connected to two copper electrodes; (*ii*) T-junction with fingertight fittings to connect tubing, a copper electrode, and a capillary; (*iii*) 50 μm inner diameter round capillary glued into a 200 μm square capillary for support; (*iv*) Syringe pump controlling the pressure by varying the flow rate of the electrolyte; (*v*) Reservoir filled with the running electrolyte and sealed using a septum.

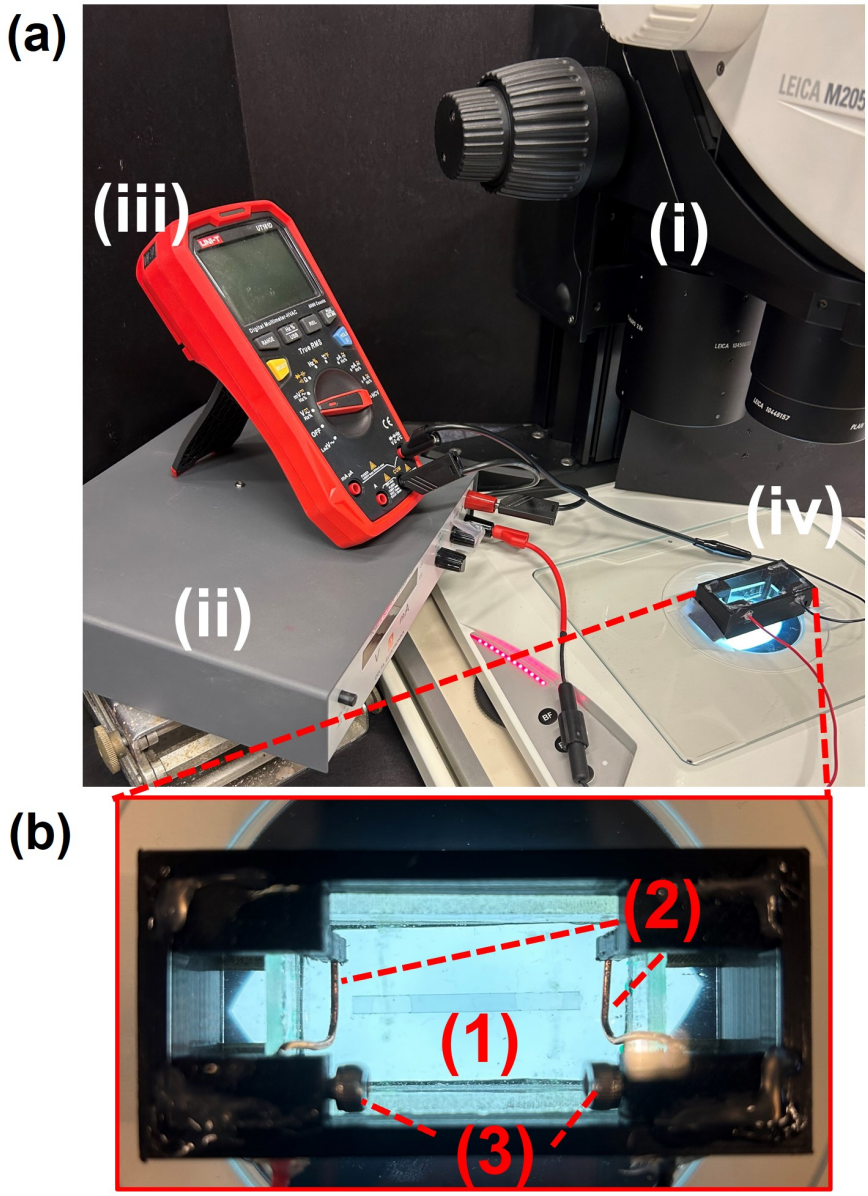

Figure 34: **(a)** Photograph showing the capillary cell setup used during measurement of the EOF through the capillary. (*i*) Microscope; (*ii*) DC power supply; (*iii*) Voltmeter connected to the DC power supply and the capillary cell; (*iv*) Capillary cell connected to the DC power supply and voltmeter. **(b)** Close-up showing a top-view of (*iv*). (1) A 2 × 0.1 mm rectangular capillary; (2) Copper electrodes; (3) Screws to fasten the copper electrodes to the frame.

Appendix B

Velocity profile of electroosmotic flow experiments

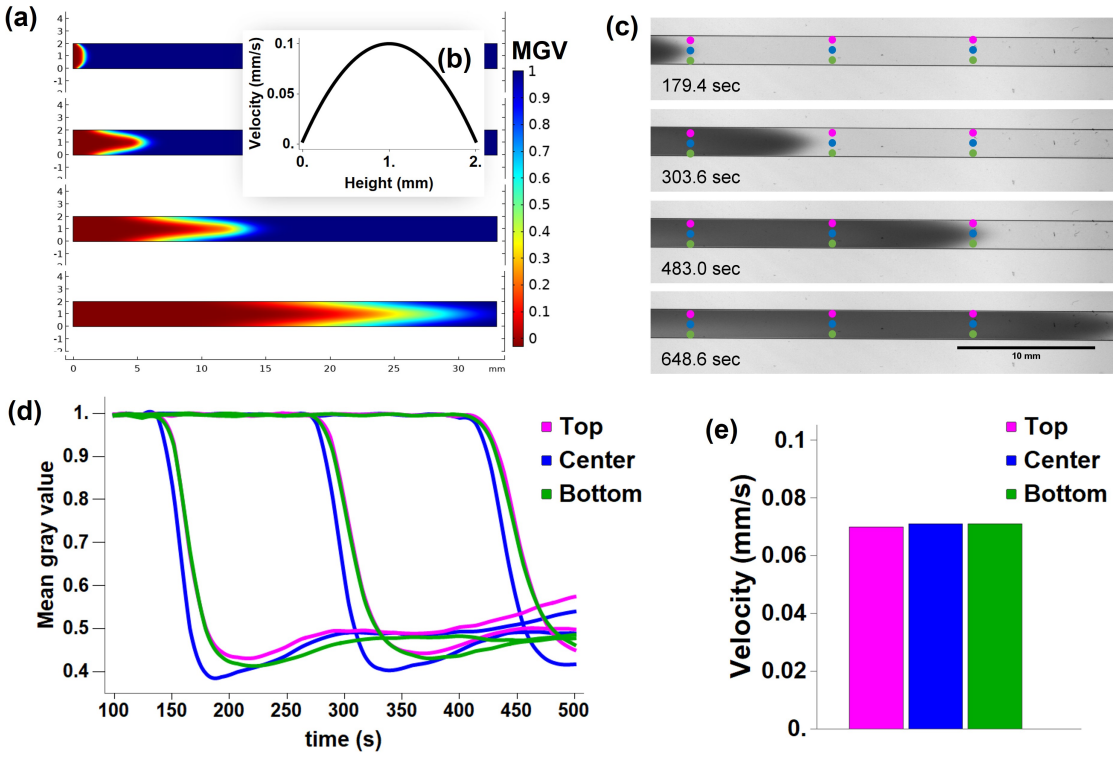

Figure 35: **(a)** Snapshots from COMSOL showing the migration of a dye through a channel under the influence of a parabolic velocity profile. **(b)** The parabolic velocity profile used in the COMSOL simulation from (a). **(c)** The migration of rhodamine B through a glass silica capillary under the influence of an electric field. **(d)** MGVs measured from (c). The colors correspond to the height in the capillary were the MGV was measured as given by the colored dots in (c). **(e)** Velocities at different heights in the capillary in (c) calculated from (b). The velocity is constant across the height of the channel.

The expected velocity profile for electroosmotic flow (EOF) is a plug flow as given in Figure 4. However, experimental data of the migration of rhodamine B through capillaries in an electric field often showed the dye-front to have a parabolic shape (Figure 35 (c)). From this it might be concluded that the velocity profile is also parabolic, which is associated with pressure driven flow.

Here, we argue that the velocity profile of the EOF experiments is indeed a plug flow. To this end a COMSOL simulations was performed to simulate the migration of a dye through a channel under the influence of a parabolic velocity profile (Figure 35 (a)). One end of the channel was given a *fully*

developed flow boundary condition with an average velocity of 0.068 mm/s. This value corresponds to the velocity measured from the migration of rhodamine B through a glass capillary under the influence of an electric field ($E = 1900$ V/m, Figure 35 (c)). The resulting parabolic velocity profile of the simulation is given in Figure 35 (b).

The dye-front under the influence of a parabolic velocity profile indeed shows a parabolic shape (Figure 35 (a)). However, the difference in velocity at different heights in the channel results in the shape of the dye-front smearing out across the channel over time. This is not observed while performing EOF experiments. The shape of the dye-front stays constant over time, indicating that the velocity at different heights in the capillary is the same. This corresponds to a plug flow.

To strengthen this qualitative observation, the MGV of the experiment in Figure 35 (c) was measured at three different positions along the channel for three different heights in the channel (Figure 35 (d)). From this the velocity at the top, center, and bottom of the capillary was determined as described in Section 3.7. This gave the velocities presented in Figure 35 (e), which are clearly constant across the height of the channel indicating a plug flow. The apparent parabolic shape of the dye-front during EOF experiments is ascribed to entrance effects of the dye entering the channel.

Appendix C

COMSOL simulations showing the velocity profile during streaming potential measurements

During streaming potential measurements a pressure is applied across a narrow channel resulting in fluid flow through the channel. Pressure driven flow is associated with a parabolic velocity profile. However, during streaming potential measurements an electric potential develops across the channel that induces an ionic current in opposing direction to the pressure driven flow. It can be expected that the ions of this current induce a flow due to drag forces exerted by the ions on the fluid. This flow will be in opposite direction with respect to the pressure driven flow. Here, a COMSOL Multiphysics model is used to understand the interplay between these two fluid flows during streaming potential measurements and the resulting velocity profile will be solved.

Model geometry, boundary conditions, and meshing

To simulate a streaming potential measurement a 2D axis-symmetrical COMSOL model was built consisting of a 10 μm long channel of radius $r = 500$ nm. A reservoir was built at either end of the channel with a radius of $R = 6$ μm and a height of 6 μm (Figure 36 (a)). The *laminar flow* module was used to simulate pressure driven flow through the channel. The *transport of diluted species* (TDS) module was used to simulate the transport of two monovalent ions of charge $z = \pm 1$ through the channel. The *AC/DC* module was used to simulate the surface charge of the inner wall of the channel and the electric potential that develops during the measurement. Table 6 summarizes the boundary conditions for each segment given in Figure 36 (a).

To simulate the streaming potential that develops across the channel it is necessary to capture the complexity of the electric double layer that extends from the charged wall in the model. This is done by dividing the channel in two regions: $r < 485$ nm and $485 < r < 500$ nm (Figure 36 (b)). This allows to refine the mesh COMSOL uses for its calculation to sub-nanometer mesh elements near the inner wall while keeping the computational time low (Figure 36 (d)). A physics-controlled *extra fine* mesh was used for the rest of the channel and the reservoirs were give a physics-controlled *normal* mesh (Figure 36 (c)).

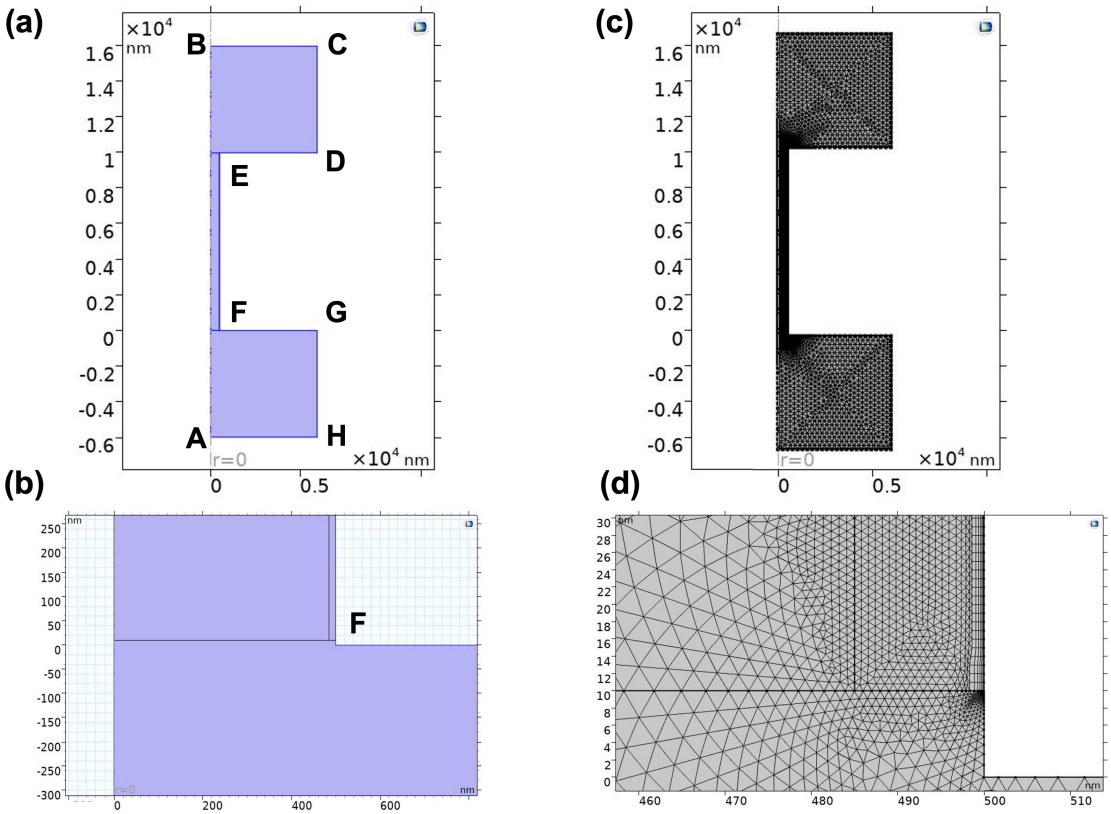

Figure 36: **(a)** Geometry used to simulate streaming potentials using COMSOL. The corners of the model are labeled $A - H$ and the boundary conditions applied to each segment are given in table 6. **(b)** Close-up of the entrance of the channel showing the two regions inside the channel. **(c)** Overview of the meshed model geometry. **(d)** Close-up of the entrance of the channel showing the refined mesh near the wall of the surface.

Table 6: Boundary conditions for the segments given in Figure 36 (a) for each module used to simulate streaming potentials.

Segment	**Laminar flow**	**TDS**	**AC/DC**
AB	Axial symmetry	Axial symmetry	Axial symmetry
BC	Oulet ($P = 0$)	Outflow	Ground ($V = 0$)
CD	Wall (no slip)	No flux	Ground ($V = 0$)
DE	Wall (no slip)	No flux	Zero charge
EF	Wall (no slip)	No flux	Surface charge density ($-2\ \mu\text{C/cm}^2$)
FG	Wall (no slip)	No flux	Zero charge
GH	Wall (no slip)	No flux	Ground ($V = 0$)
HA	Inlet ($P = 10$, 15, 20, 30 kPa)	Inlet ($c = 1$ mM for $z = \pm 1$)	Ground ($V = 0$)

Velocity profile

The COMSOL model described above was used to investigate the velocity profile during streaming potential measurements. Figure 37 (a) gives a surface plot of the velocity inside the channel when applying a pressure of 15 kPa. The radial velocity profile is plotted in Figure 37 (b) and shows a parabolic profile.

From this it could be concluded that the model does not accurately simulate the streaming potential, however this is not the case. Figure 37 (c) shows a surface plot of the electric potential that develops across the channel when applying a 15 kPa inlet pressure. Clearly a streaming potential is simulated. The model is also able to capture the electric double layer that extends from the charged surface into the solution as shown in Figure 37 (d).

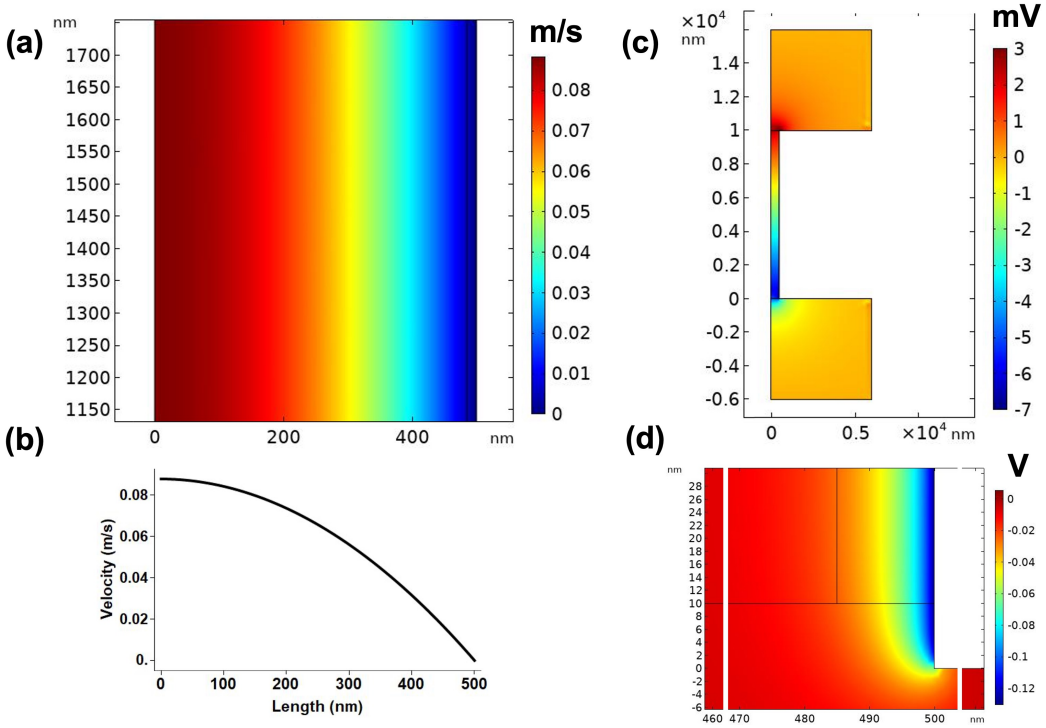

Figure 37: **(a)** Surface plot of the velocity in the channel of the COMSOL model for an inlet pressure of 15 kPa. **(b)** Radial velocity profile corresponding to (a). **(c)** Surface plot of the electric potential showing the streaming potential that develops across the channel. **(d)** A surface plot of the electric potential showing a close-up of the entrance of the channel near the channel wall. The model is able to capture the electric double layer that extends from the charged surface into the bulk.

It was concluded that any flow induced by the movement of ions due to the development of a streaming potential is negligible. An estimate was made of the velocity of the counter flow to confirm this. The counter flow is

expected to be an electroosmotic plug flow, which by approximation shows a constant velocity across the radius of the channel. The magnitude of the velocity can be calculated if the electroosmotic mobility is known. To this end, the potential across the segment AB was plotted for different inlet pressures (Figure 38 (a)). The streaming potential was calculated by taking the difference between the maximum and the minimum value of the potential across segment AB. The streaming potentials were plotted against the inlet pressures and from the slope of the linear fit a zeta-potential of $\zeta = -9$ mV was calculated using Equation (7). From this, an electroosmotic mobility of $\mu_{EO} = 6.37 \times 10^{-9}\ \mathrm{m^2\,V^{-1}\,s^{-1}}$ was calculated using Equation (6).

The velocity of the electroosmotic counter flow can now be calculated for an inlet pressure of 15 kPa. At this pressure a streaming potential of $U_{str} = 8.2$ mV develops across the channel, giving an electric field of $E = 823$ V/m. It follows from Equation (6) that this gives a counter flow with a velocity of $v_{counter} = 5.2 \times 10^{-6}$ m/s. This is far less than 1% of the maximum velocity of the pressure driven flow at 15 kPa: $(5.2 \times 10^{-6}/0.09) \times 100\% = 0.006\%$. It can thus be concluded that the velocity profile during streaming potential measurements is completely dominated by the pressure driven flow and any counter flow can be neglected.

This also becomes apparent when the model is used to simulate purely pressure driven flow, without any transport of species and electric potentials. Comparing the radial velocity profile of this pressure driven flow at 15 kPa with the velocity profile found for streaming potential simulations shows that they are indistinguishable (Figure 39).

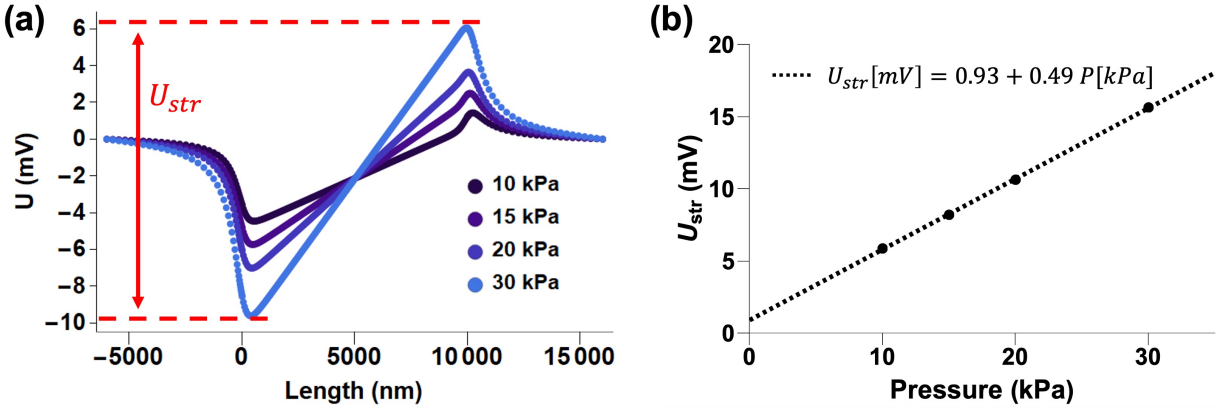

Figure 38: **(a)** The electric potential U across the segment AB for different inlet pressures. The streaming potential U_{str} was determined from the difference between the maximum and minimum value of the potential across segment AB indicated by the dashed red lines for $P = 30$ kPa. **(b)** The streaming potentials determined from (a) plotted against the inlet pressure. From the slope of the linear fit the zeta-potential is calculated.

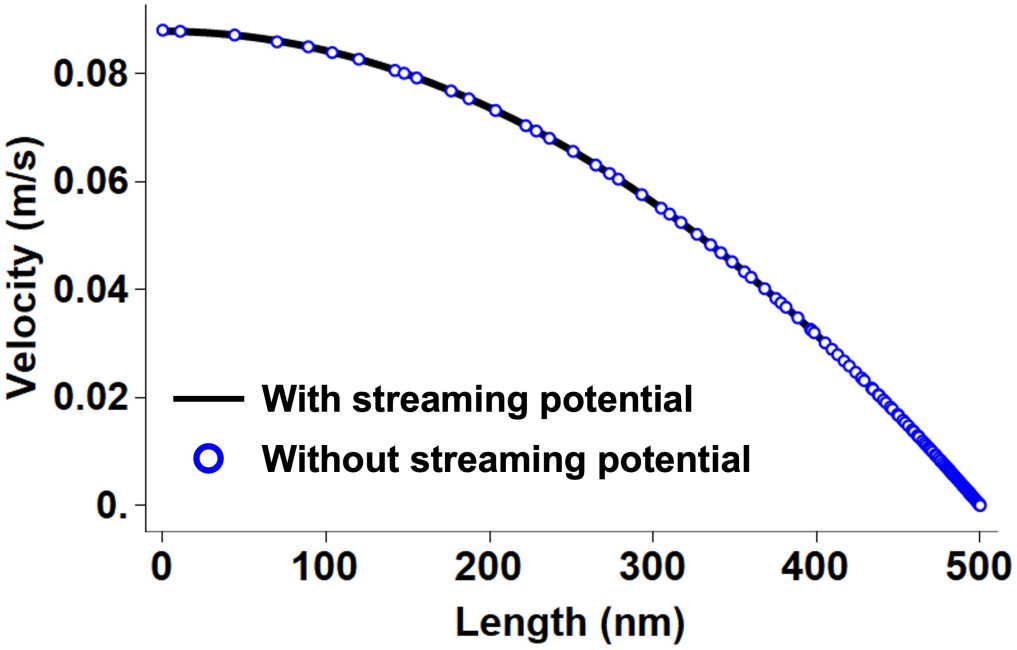

Figure 39: Comparison between the simulated radial velocity profiles of pressure driven flow through a channel with and without the development of a streaming potential. The inlet pressure for both simulations was 15 kPa.